Building a bridge between comparable and extreme mass ratio black hole binaries: A single spin precessing model for the final state

Maria de Lluc Planas,[1] Joan Llobera-Querol,[1] and Sascha Husa[2,1]
[1]*Departament de Física, Universitat de les Illes Balears, IAC3—IEEC, Carretera de Valldemossa km 7.5, E-07122 Palma, Spain*
[2]*Institut de Ciències de l'Espai (ICE, CSIC), Campus UAB, Carrer de Can Magrans s/n, 08193 Cerdanyola del Vallès, Spain*

(Received 2 February 2024; accepted 10 May 2024; published 11 June 2024)

Modeling the gravitational wave signal from binaries beyond comparable mass is an important open issue in gravitational wave astronomy. For nonspinning binaries and when the spins are aligned with the orbital angular momentum, some first studies concerning the transition between the comparable and extreme mass ratio regime are already available, which suggest that extreme mass ratio results at times extrapolate to comparable mass ratios with surprising precision. Here we study the case of misaligned spins: We present new numerical relativity (NR) simulations performed with the Einstein Toolkit code at mass ratios up to 18 and construct a heterogeneous dataset that spans all mass ratios, including data from NR simulations, numerical approximations to extreme mass ratio binaries, and data from the geodesic approximation. As a first application we provide fits for the remnant mass and spin magnitude in single spin precessing systems, omitting consideration of the in-plane spin orientation. These fits demonstrate accuracy comparable to the state-of-the-art NRSur7dq4EmriRemnant model, all while retaining the simplicity and efficiency inherent in previous phenomenological fits.

DOI: 10.1103/PhysRevD.109.124028

I. INTRODUCTION

The Laser Interferometer Space Antenna (LISA) mission is expected to observe gravitational waves from compact binaries with a large range of mass ratios [1,2] up to and including extreme mass ratio inspirals (EMRIs). It will be prudent to develop waveform models that accurately describe a wide range of mass ratios well before the LISA era and to optimize LISA data analysis algorithms with such pipelines in hand. EMRI waveforms are best described via the self-force method, where one perturbs in the mass ratio of the system ([3,4], see [5] for discussion). For comparable mass binaries, several families of waveform models have been developed [6–13], which have become indispensable tools for gravitational wave data analysis, e.g., [14–17]. Such waveform models are calibrated to data from numerical relativity (NR) simulations [18–20]. However, for the foreseeable future, NR waveforms will be sparse in the parameter space of precessing (even more so for generic) black hole binaries, especially at high mass ratios (see [21–25] for the latest releases of NR catalogs). While simulations at, say, mass ratios of order 10^2 or 10^3 are, in principle, feasible in numerical relativity [26], the number, length, and accuracy of such waveforms will be severely restricted by computational cost until new computational approaches are developed (see, however, [27]).

It is well known that the extreme mass ratio limit and the self-force expansion in mass ratio can provide useful information even for the comparable mass ratio regime [28–30], fueling hope that using such information can reduce the number of NR waveforms that are needed for calibrating waveform models. To date, work that connects the two mass ratio regimes has focused on either nonspinning binaries [31–33], the use of extreme mass ratio waveforms to calibrate quasicircular aligned spin waveform models [10,11,34,35], or the simpler problem of models for the final mass and spin in the quasicircular aligned spin case [36]. For misaligned spins, however, one faces much more complicated phenomena and a much larger parameter space (seven instead of three dimensions in the absence of orbital eccentricity, as is the case here).

In this work, we make a first step to bridge the comparable mass and extreme mass ratio regimes in the misaligned spin sector and develop precessing models for the remnant mass and spin, thus extending previous work [36] to the precessing case. An efficient and accurate remnant model for precessing systems is a key component for the advancement of precessing waveform models. Specifically, given that the ringdown frequencies are entirely characterized by the final state of the binary, remnant models play a vital role in conducting tests of general relativity through ringdown studies. Other recent remnant models in the literature include aligned spin

datasets with and without information from the extreme mass ratio (EMR) limit (see, for instance, Refs. [36,37]), precessing datasets with information from the aligned spin EMR limit (see [38,39]), surrogate models like NRSur7dq4EmriRemnant [40], and also a machine learning approach [41].

As our input data we construct a heterogeneous dataset for quasicircular precessing binaries. The dataset combines NR waveforms from different codes, numerical solutions of the Teukolsky equation [42,43], and information from Kerr geodesics [44]. To understand the region where no NR information is available, we rely on Kerr geodesics, which determine the final mass and spin to linear order in the mass ratio, but surprisingly provide valuable information across the parameter space, i.e., from EMRIs to comparable mass binaries.

In order to construct our model, we have to compensate for the lack of a dense dataset of numerical relativity simulations across a large range of mass ratios with several simplifications and approximations. As more simulations become available, along with further self-force results and possibly other analytical methods, these simplifications and approximations can be relaxed. As a first simplification, we restrict the models to the single spin case and leave double spin effects for future work. Neglecting the spin of the smaller black hole, which is a subdominant effect for large mass ratios, simplifies our analysis toward focusing on the transition to large mass ratios. Furthermore, we neglect the dependence of the angle of the spin in the orbital plane, which we will denote ϕ_1 below, for our models of the remnant mass and spin. While this angle is indeed an essential parameter for the recoil [45], and more accurate models of the mass and spin should take this dependence into account, we argue in Sec. III that we can neglect it for the simple models we present here. Further approximations are used to establish a common parametrization for our inhomogeneous nature of our input dataset. Different numerical relativity codes use different coordinate gauges, which affects, in particular, spin angles or quantities such as merger times. The geodesics and numerical solutions of the Teukolsky equation again use different coordinates. In the future it will be interesting to better understand how to remove some of the ambiguities and gauge dependencies. For this work, we justify not resolving these issues by the fact that the resultant remnant model proves to be accurately predictive and can be used for the advancement of existing waveform models. Further justifications regarding the approximations we use will be given as we introduce them throughout this paper.

In Sec. II we describe the datasets we use and the procedures chosen to blend them into a single consistent dataset. In the quasicircular aligned spin case, generating a heterogeneous dataset is relatively straightforward, since the intrinsic parameters only consist of the masses and spins, which in turn depend only very weakly on time due to the very small amounts of infalling radiation. Hence, the time dependence of masses and spins is often neglected in aligned spin waveform models [34,35]. For misaligned spins, however, the spin angles and orientation of the orbital plane depend on time, and a coordinate frame needs to be defined judiciously to consistently parametrize the different datasets. Note that throughout this paper we refer to any black hole binary system without in-plane spin contributions as having "aligned spin" (AS), independent of whether spins are parallel or antiparallel to the orbital angular momentum.

In Sec. III we use our heterogeneous dataset to compute the remnant mass and spin magnitude across all mass ratios for the case when only the larger black hole is spinning, as the spin on the smaller black hole becomes a subdominant effect for large mass ratios [46]. Additionally, we neglect the orientation of the in-plane component of the single spin, a decision driven by the current limitations in computational cost and tests of the impact of the in-plane angle on our results. Ultimately, a careful selection of the quantities for modeling allows us to generate simple parametrized fits for both the mass and spin magnitude of the remnant in a precessing binary. These fits can be evaluated efficiently and achieve an accuracy comparable to the NRSur7dq4EmriRemnant model [40], the current state of the art in remnant models.

Finally, in Sec. IV, we summarize and discuss the scope and limitations of the work we report here, as well as next steps.

Throughout this paper, we use geometric units with $G = c = 1$. Component masses are denoted by m_i, and we define the mass ratio $q = m_1/m_2 \geq 1$ and the symmetric mass ratio $\eta = m_1 m_2/(m_1 + m_2)^2$. The total component mass will be denoted by $M = m_1 + m_2$ and will serve as a scale parameter. The dimensionless spin magnitudes are denoted χ_i.

II. PRECESSING DATASET

In Secs. II A and II B we review the ingredients for our heterogeneous dataset:

(i) NR waveforms from the public SXS catalog [22], produced with the SpEC code [47], and the Cardiff group's public catalog [23] of waveforms produced with the BAM [48,49] code;
(ii) NR waveforms recently produced with the public Einstein Toolkit code [50], which have not been presented previously;
(iii) numerical solutions of the Teukolsky equation for inspirals at mass ratio 1000 [42,43]; and
(iv) solutions of the geodesic equation in Kerr spacetime.

In Sec. II C we discuss how to blend all the above data into one consistent dataset for the remnant mass and spin.

Our datasets use different coordinate gauge conditions, and thus spin angles cannot be expected to be exactly the same even for physically identical binaries. We expect such

uncertainties to only correspond to a few degrees [51] and to not play a major role at our current level of accuracy. In our work, we again find approximate consistency between different datasets; this aspect will, however, have to be studied further in the future.

A. NR datasets

Our NR dataset spans mass ratios from $q = 1$ (equal masses) to $q = 18$. We use data from two publicly available catalogs of NR simulations, the SXS catalog [22], obtained with the SpEC code [47], and a catalog of waveforms [23] obtained with the BAM code [48,49]. In addition we use new simulations we performed with the Einstein Toolkit (ETK) [50]. The SXS simulations are performed with the generalized harmonic formulation of the Einstein equations [52], while the BAM and ETK simulations use the moving puncture setup with the $1 + \log$ lapse and $\tilde{\Gamma}$-driver shift coordinate conditions. We have analyzed both the waveforms and apparent horizon data of all simulations to create a consistent heterogeneous dataset encompassing information from both sources. In this paper, however, we only discuss the remnant properties, leaving investigations into the precessing waveform dataset to future work.

All the NR points in our dataset are included in Fig. 1, where we show the distribution of the data in a three-dimensional subspace defined at $100M$ before merger. The merger time is not defined in exactly the same way for data produced with different codes. We report details for each catalog in the subsections below, however, our findings indicate that the small differences in the definition of the merger time across catalogs does not significantly impact the results at the current level of accuracy. For all datasets, we shift the time coordinate to the value of zero at the merger time. From Fig. 1 we can see that the majority of the points are concentrated in the comparable mass regime ($\eta \geq 0.15$), mostly from the SXS catalog. The BAM points are located in the lower plane as they are single spin simulations, while the high mass ratio ETK simulations are dispersed in the mid–high mass ratio regime. In Fig. 2 we show the single spin simulations distributed in the (η, χ_1, θ_1) parameter space, where χ_1 is the magnitude of spin of the more massive black hole, and θ_1 is the angle between the spin and the axis of orbital motion $100M$ before merger. These are the simulations we are using to compute the remnant fits in Sec. III.

1. SXS dataset

We use 1409 quasicircular precessing simulations from the SXS catalog [22], which range from mass ratio 1–6 and $0 < \chi_1 < 0.99$, $0 < \chi_2 < 0.9$. To confine the parameter space to quasicircular orbits, we impose a limit on the orbital eccentricity e (effectively defined as the Newtonian eccentricity, see [22]) to $e \leq 0.002$, leading to the exclusion of 13 simulations from the original catalog. The reference_eccentricity parameter from the metadata was utilized for this purpose. Among the 1409 simulations included in our analysis, 80 correspond to single spin configurations. The criterion for identifying single spin cases was

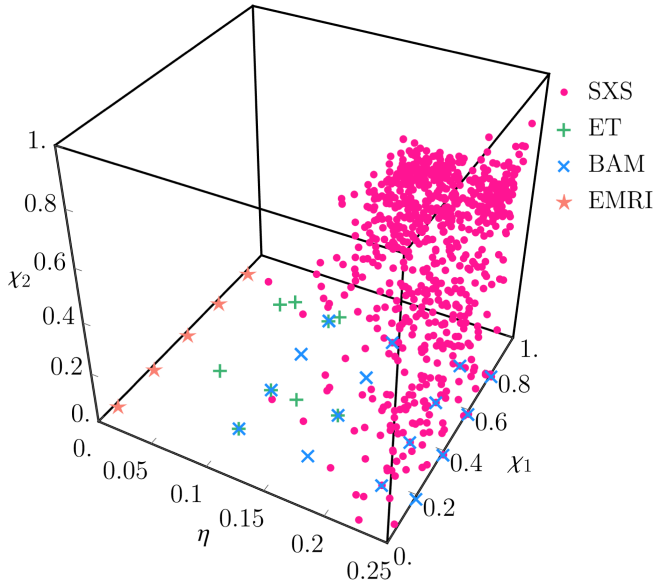

FIG. 1. Three-dimensional representation of the precessing numerical relativity simulations used in this project described in Sec. II. The visualization presents the distribution of the data in terms of their symmetric mass ratio η and the spin magnitudes of the largest and smallest black holes, denoted as χ_1 and χ_2, respectively.

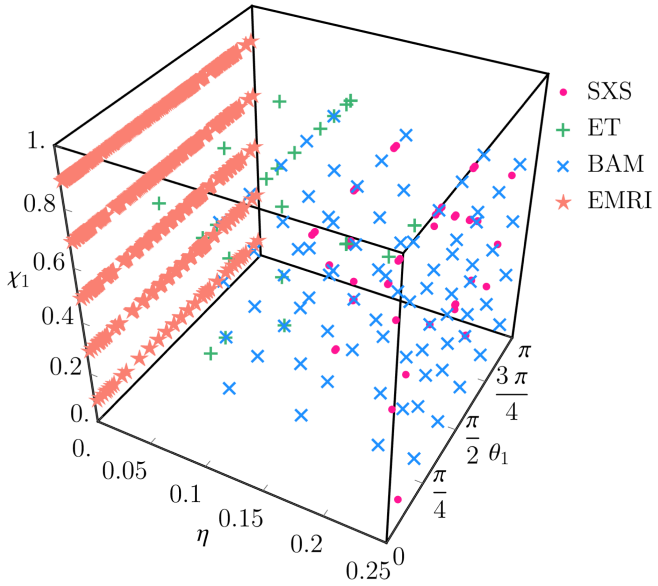

FIG. 2. Three-dimensional representation of the single spin subset of the precessing numerical relativity simulations introduced in Sec. II. It shows the distribution of the data in terms of their symmetric mass ratio η, the spin magnitude of the largest black hole χ_1, and its orientation with respect to the orbital frequency vector at the reference time θ_1.

$\chi_2(t_{\rm ref}) < 0.001$. These specific waveforms are employed for the remnant properties' fits presented in this paper, with the reference time set at $t_{\rm ref} = -100M$ (where the merger corresponds to $t = 0$). For the SXS dataset the merger time is defined as the maximum of the L^2 norm of all the available modes, as provided by the SXS PYTHON package.

The simulations have been performed with the pseudospectral SpEC code [47], which excises spatial regions inside of pure outflow boundaries located inside but close to the apparent horizons of the black holes. Initial data are constructed to satisfy the constraints of general relativity using the extended conformal thin sandwich [53,54] equations.

2. BAM dataset

We also use 80 simulations from the single spin Cardiff precessing catalog [23], which span the $1 \leq q \leq 8$, $0 < \chi_1 < 0.8$, $\chi_2 = 0$ parameter space evenly in mass ratio, spin magnitude, and orientation θ_1, so $\theta_1(t_{\rm in}) \in \{\frac{\pi}{6}, \frac{\pi}{3}, \frac{\pi}{2}, \frac{2\pi}{3}, \frac{5\pi}{6}\}$. The in-plane orientation of the single spin ϕ_1 was chosen to be zero at the relaxed time for each simulation. The eccentricity for all the simulations was reduced to 0.002 through manual iterations of the linear momenta of the punctures in the initial parameters (see Sec. II B 1 in [23] for details). For the BAM dataset, the merger time is defined to be the peak of the $l = 2$ multipole modes of Ψ_4, provided in the metadata.

The simulations have been carried out in the "moving puncture" approach with the BAM code, which uses conformally flat Bowen-York puncture initial data [55]. Note that this setup for the initial data allows one to analytically compute the initial orbital angular momentum analytically using the Newtonian physics formula as a cross product of position vector and linear momentum. The initial data are evolved with fixed mesh refinement and sixth order finite differencing [48,49].

3. Einstein Toolkit dataset

In addition to the public data from the SXS and BAM dataset, we also use higher mass ratio simulations we have recently performed with ETK [50]. We produced 24 simulations that span the region $4 \leq q \leq 18$, $0.4 \leq \chi_1 \leq 0.8$, $0 \leq \chi_2 \leq 0.4$. Because of an inappropriate configuration of the wave extraction grids, some gravitational wave signals exhibit excessive noise, making it challenging to extract the merger time directly from it. We thus rely on horizon quantities, identifying the merger time as the transition from the individual black hole spins to the remnant spin. Detailed information on these simulations can be found in Table I.

The setup of our Einstein Toolkit code is very similar to that of the BAM code. Differences include the use of eighth order accurate finite difference stencils and the eccentricity reduction algorithm described in [56]. Furthermore, fixed mesh refinement with moving cubical boxes is not used for the whole computational domain. However, for the wave extraction region and beyond, the multipatch Llama code [57] is used to allow a high radial grid resolution with a reduced memory consumption. The final mass and spin are determined from the apparent horizons, which are located with the AHFinderDirect code [58].

B. Extreme mass ratio limit

In the EMR case ($\eta \ll 1/4$) one can rely on black hole perturbation theory (BHPT), which assumes a perturbation of Kerr spacetime due to a small object m_2 orbiting a black hole of mass $m_1 \gg m_2$. In the test mass limit ($\eta \to 0$) the calculation of the orbital motion decouples from the calculation of the gravitational wave signal, radiation reaction vanishes, and the smaller object follows a geodesic. Below we first summarize quasicircular geodesics of Kerr spacetime and then describe our numerical dataset for mass ratio 10^3 [42], which we use for cross-checks.

1. Kerr geodesics

We consider the geodesic motion of a test mass m_2 in a Kerr spacetime of mass m_1 and angular momentum $|J| = am_1$. For a given black hole with parameters a and m_1 the geodesics can be parametrized by the constant orbital quantities p (semilatus rectum), e (eccentricity), and θ_- (inclination parameter), or by the energy E, angular momentum along the axis of symmetry L_z and Carter's constant Q, which are also constants of motion. The orbital quantities are defined in Boyer-Lindquist coordinates (t, r, θ, φ) [59]. In this paper, we will only be interested in the circular case, where $e = 0$ and radial separation r is constant, while the angular position θ will be time dependent and oscillates between extrema determined by the inclination parameter θ_-,

$$\theta_- \leq \theta \leq (\pi - \theta_-). \tag{2.1}$$

The solution for the time-dependent geodesic motion, and the relation between the conserved quantities (E, L_z, Q) and the orbital motion can be found, for instance, in Ref. [44], and is briefly summarized in Appendix A. Here we follow the parametrization of [44] or [60], which is also used in the Black Hole Perturbation Toolkit software package [61]. This toolkit, among other things, provides a *Mathematica* implementation of Kerr geodesics, KerrGeodesics, which we have used in parallel to our own implementation. In order to solve for the geodesics and discuss the results, it is natural to adopt a scale-invariant formulation of the problem introducing dimensionless quantities,

$$\tilde{a} = \frac{a}{m_1}, \quad \tilde{E} = \frac{E}{m_2}, \quad \tilde{L_z} = \frac{L_z}{m_1 m_2}, \quad \tilde{Q} = \frac{Q}{{m_1}^2 {m_2}^2}. \tag{2.2}$$

The conserved quantities $(\tilde{E}, \tilde{L}_z, \tilde{Q})$ can be computed algebraically from the parameters (a, p, e, θ_-), e.g.,

TABLE I. Initial and reference data (in brackets) of the numerical relativity simulations computed using the Einstein Toolkit, described in Sec. II A 3. The reference time is chosen to be $100M$ before merger. From left to right, the table gives the ID of each simulation, its mass ratio, the dimensionless spin magnitude of the larger black hole, the primary spin's orientation with respect to the orbital frequency $\vec{\omega}$, the dimensionless spin of the lighter black hole, its orientation, the dimensionless orbital frequency at which the quantities are given, the dimensionless final mass of the remnant object, its spin, its orientation with respect to $\vec{\omega}$, and finally, the dimensionless merger time.

ID	q^{ref}	χ_1	$\theta_{\mathrm{L}\chi_1}$ (deg)	χ_2	$\theta_{\mathrm{L}\chi_2}$ (deg)	$M\omega_{\mathrm{orb}}(\times 10^{-2})$	M_f/M	χ_f	$\theta_{\mathrm{L}\chi_f}$ (deg)	t_{M}/M
1	4	0.4	135.0 (134.1)	0	⋯	1.66 (5.44)	0.981	0.368	17.27 (27.89)	2562
2	4	0.4	170.0 (170.0)	0	⋯	1.66 (5.29)	0.982	0.265	6.41 (9.51)	2395
3	4	0.4	170.0 (169.8)	0.4	170.0 (170.1)	1.64 (5.18)	0.982	0.257	7.20 (10.14)	2328
4	6	0.4	135.0 (134.1)	0	⋯	1.98 (5.35)	0.987	0.281	36.34 (46.30)	2555
5	6	0.4	135.0 (133.5)	0.4	135.0 (145.1)	1.96 (5.31)	0.987	0.283	37.67 (47.30)	2504
6	8	0.8	170.0 (169.5)	0	⋯	1.86 (4.83)	0.992	0.285	155.1 (156.7)	2016
7	8	0.4	90.00 (88.24)	0	⋯	2.06 (6.32)	0.989	0.440	36.77 (43.76)	2253
8	8	0.8	135.0 (135.1)	0	⋯	1.89 (5.21)	0.991	0.460	92.79 (100.7)	2433
9	8	0.8	90.00 (86.03)	0	⋯	2.13 (6.54)	0.986	0.700	58.90 (59.14)	2362
10	8	0.8	170.0 (169.9)	0	⋯	1.92 (4.80)	0.992	0.285	155.0 (157.1)	2016
11	8	0.4	15.00 (14.89)	0	⋯	2.49 (7.17)	0.986	0.585	6.81 (7.67)	1605
12	8	0.2	90.00 (89.98)	0	⋯	2.63 (6.07)	0.989	0.345	24.25 (27.09)	1047
13	8	0.4	30.00 (29.14)	0	⋯	2.49 (7.05)	0.986	0.573	13.45 (14.69)	1574
14	8	0.8	165.0 (164.5)	0	⋯	2.19 (4.70)	0.992	0.301	144.9 (146.3)	1307
15	8	0.8	15.00 (15.13)	0	⋯	2.61 (9.05)	0.977	0.858	9.64 (10.61)	1906
16	8	0.8	150.0 (149.2)	0	⋯	2.24 (4.84)	0.992	0.372	117.6 (120.5)	1274
17	8	0.8	30.00 (27.55)	0	⋯	2.58 (8.72)	0.978	0.847	19.33 (18.14)	1895
18	8	0.8	75.00 (74.63)	0	⋯	2.62 (6.87)	0.984	0.757	49.34 (52.04)	1368
19	8	0.8	105.0 (104.1)	0	⋯	2.47 (5.81)	0.989	0.633	68.37 (74.24)	1320
20	18	0.4	150.0 (149.9)	0	⋯	2.51 (5.64)	0.996	0.225	124.5 (126.8)	2234
21	18	0.4	90.00 (89.34)	0	⋯	2.74 (6.63)	0.996	0.395	61.30 (65.03)	2221
22	18	0.8	150.0 (149.4)	0	⋯	2.39 (5.00)	0.996	0.565	138.7 (139.8)	2207
23	18	0.8	30.00 (29.78)	0	⋯	2.93 (10.5)	0.991	0.828	24.33 (25.20)	3243
24	18	0.8	90.00 (90.35)	0	⋯	2.87 (6.93)	0.995	0.738	75.84 (77.67)	2243

$$\tilde{Q} = \cos^2\theta_- \left[\tilde{a}^2(1-\tilde{E}^2) + \frac{\widetilde{L_z^2}}{1-\cos^2\theta_-}\right]. \quad (2.3)$$

The Carter constant is given by $Q = L^2 - L_z^2$ in the limit $a \to 0$. It is, however, useful to approximate L_ρ by the square root of the Carter constant $\sqrt{Q}$ even for nonvanishing spin, see, e.g., [60]. There, an equivalent inclination angle I (called θ_{inc} in [60]) is defined as

$$I = \frac{\pi}{2} - \mathrm{sign}(L_z)\theta_-, \quad (2.4)$$

which resembles an alternative definition for an orbital inclination angle ι,

$$\cos\iota = \frac{L_z}{\sqrt{L_z^2 + Q}}, \quad (2.5)$$

where Q plays the role of the magnitude squared of the angular momentum orthogonal to L_z. It has been found that, in general, $\iota \approx I$ and that the angles I and ι automatically encode a notion of prograde and retrograde orbits ($I, \iota < 90°$ for prograde and $I, \iota > 90°$ for retrograde) [44]. In terms of the energy and angular momentum, one finds that $\tilde{E}^{(p)} < \tilde{E}^{(r)}$ and $\tilde{L_z}^{(p)} < \tilde{L_z}^{(r)}$, where p stands for prograde orbits and r for retrograde, i.e., for prograde orbits the particle has higher binding energy.

Of special interest is the innermost stable spherical orbit (ISSO). Particles with small but finite mass will adiabatically inspiral to the ISSO and then plunge into the black hole. The radiation of energy and angular momentum during the plunge is much smaller than during the inspiral, and the remnant mass and spin can therefore be approximated by the values of the energy and angular momentum at the ISSO. This aspect will be discussed further in Sec. III and concretely motivated in Fig. 5.

The simpler subset of aligned spin binaries is defined by setting the inclination angles I or ι to 0 or π. The L_z component of the orbital angular momentum then corresponds to the total orbital angular momentum, the final spin only has a nonvanishing z component, and the orbital plane is preserved. In this particular case of equatorial orbits, the ISSO is referred to as innermost stable circular orbit (ISCO).

2. Numerical EMRI data

In this work we use the data of [42], 5925 EMRIs of mass ratio $q = 1000$, distributed in a grid of values of the

spin of the largest black hole a, inclination angle I, and plunge angle θ_f (see Fig. 3). Reference [42] extends the work of Ori and Thorne [62] from equatorial to inclined orbits. The procedure splits the worldline into three regions: (i) The adiabatic inspiral, where they use a frequency-domain BHPT code [60] to evolve the orbital quantities until they reach (ii) the transition region. Closer to the ISSO, the inspiral is no longer adiabatic, requiring further considerations. (iii) On reaching the plunge, E, L_z, and Q are frozen to the last value of the orbit while other orbital quantities are evolved solving the geodesic equation. We thus define the merger time when the small object crosses the horizon and E, L_z, and Q reach their frozen value.

In Lim *et al.* [43], the companion paper to [42], they investigate the dependence of individual-mode excitation on plunge parameters via their waveform set. The gravitational waves generated by the system are computed from the worldline by solving the Teukolsky equation in the time domain [63,64]. Further details on the procedure can be found in Ref. [42].

For each configuration, the dataset includes all the spherical harmonic modes up to $l = 4$, plus selected higher l, m modes, and complete information on the small body's trajectory,

$$\vec{x_2}(t) = -\vec{r} = r(t)(\sin\theta(t)\cos\phi(t), \sin\theta(t)\sin\theta(t), \cos\theta(t)), \tag{2.6}$$

by providing (r, ϕ, θ), velocity $(\mathrm{d}r/\mathrm{d}t, \mathrm{d}\phi/\mathrm{d}t, \mathrm{d}\theta/\mathrm{d}t)$, and also the time evolution of the geodesic constants of motion E, L_z, and Q, which are used in Sec. II C 2 to compute the remnant quantities. The natural frame for EMRIs is defined by the spin of the massive black hole, so both the waveform and trajectories are defined with respect to this frame as illustrated in Fig. 3. To cohesively append to our existing dataset, it is therefore necessary to transform from this frame to that used by comparable mass simulations, where the z axis is defined not by the angular momentum of the larger black hole, but by the direction of the orbital angular momentum or a similar quantity like the orbital angular velocity or Newtonian orbital angular momentum $\vec{\omega}$, as shown in Fig. 4.

C. Creation of a heterogeneous dataset

In this work, we investigate the properties of the remnant object: the final mass and spin. The final mass of the binary is given by

$$M_f = 1 - E_{\mathrm{rad}}, \tag{2.7}$$

and one can then apply the conservation of angular momentum to compute the final spin $\vec{\chi}_f$,

$$M_f^2\vec{\chi}_f = m_1^2\vec{\chi}_1 + m_2^2\vec{\chi}_2 + \vec{L}. \tag{2.8}$$

For the numerical relativity datasets, the final mass and spin were determined from the apparent horizons. In the case of the SXS and BAM dataset they were taken from the supplied metadata, and for our Einstein Toolkit dataset the numbers were averaged over appropriate portions of the late time behavior of the dataset. For the extreme mass ratio case, the determination of the final state is described below.

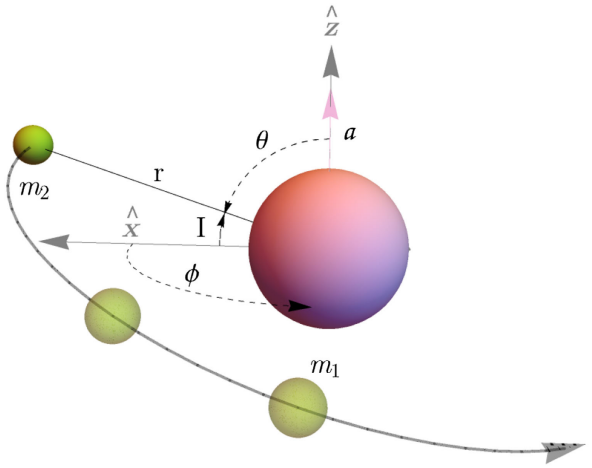

FIG. 3. Definition of the EMRI orbital quantities provided in the dataset described in Sec. II B. The dataset spans a parameter space described by the black hole spin magnitude a, the inclination angle I, and the final angle of the plunge θ_f. The spherical coordinates (r, θ, ϕ) determine the evolved position of the smaller black hole of mass m_2.

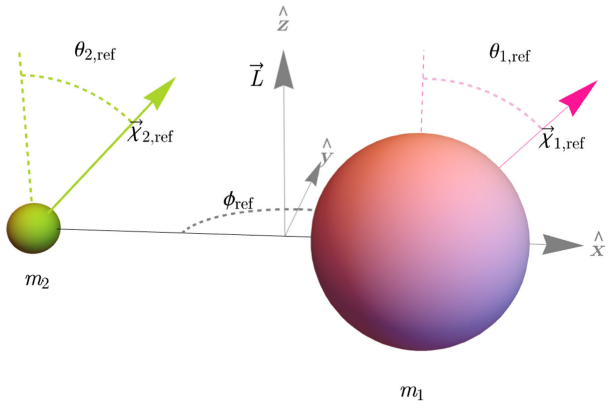

FIG. 4. Definition of the orbital quantities employed in this project (traditional to the comparable mass simulations). All vectors are defined with respect to the orbital angular momentum $\vec{L}$, as opposed to those shown in Fig. 3, which are specified in terms of the larger black hole spin. Note that in this project we approximate $\vec{L}$ by $\vec{\omega}$ (2.9).

1. Choice of reference frame

In the aligned spin quasicircular sector, creating a consistent heterogeneous dataset, which combines comparable mass and extreme mass ratio cases, is relatively straightforward. As the spins and orbital plane maintain their orientation as a consequence of equatorial symmetry, a natural class of inertial frames can be constructed, where the z axis is the fixed axis of the orbital motion, and the angular coordinate in the orbital plane can be defined based on the separation vector. In the precessing case, this equatorial symmetry of the aligned spin vector is lost; the orbital plane and spin directions are time dependent and there is, in general, no natural inertial frame. An intuitive approach to choosing a reference frame is then to work with a noninertial frame that tracks the precession motion, which drastically simplifies the dynamics and waveform [65,66]. This can then be used to construct precessing waveform models in terms of rotating or "twisting up" a nonprecessing waveform with an inverse rotation that maps a corresponding precessing waveform into the appropriate noninertial frame [65,66]. Unfortunately, the natural choices in the EMR limit and comparable mass cases are not equal.

For EMRIs, as discussed above in Sec. II B, fixing an inertial frame by choosing the z axis as the spin axis of the large black hole (BH) is indeed natural, e.g., it gives rise to a conserved spin component in the z direction of the larger BH, a conserved orbital angular momentum projection L_z, and the definition of the conserved inclination I for a fixed geodesic. In the comparable mass case, this choice has, however, no meaningful analog, and it has become customary to work in a co-orbital or similar frame, which is defined in the spirit of the quadrupole aligned frame [65–67] for the gravitational wave signal. Similar behavior can be achieved by choosing the z axis as the direction of the orbital angular momentum $\vec{L}$ or the orbital angular velocity $\vec{\omega}$. In the frame defined by the orbital angular momentum, the magnitude of the spin projections parallel and orthogonal to the orbital angular momentum are approximately preserved [68,69] and the orbital angular momentum is approximately aligned with the direction of maximum wave emission [65]. In the EMR limit, the projection of the black hole spin onto the orbital angular momentum is preserved, in contrast to the scenario where the orbital angular momentum is replaced the orbital angular velocity $\vec{\omega}$. Some simplification of the gravitational wave signal and dynamics can also be achieved by choosing the z axis as the direction of the total angular momentum $\vec{J}$, see, e.g., [66], which only varies slowly and by a small amount, except for the case of transitional precession [66]. Furthermore, in the EMR limit, $\vec{J}$ corresponds to the spin of the largest black hole, making it a more suitable choice as the mass ratio increases.

The NRSur7dq4 model [12] uses the quadrupole aligned waveform to define the reference frame, where the z axis is computed as the principal eigenvector of the angular momentum operator as described in [67]. In this work, we have chosen to construct our co-orbital frame in terms of orbital quantities, as their formulation is more straightforward than the orbital angular momentum in a numerical relativity evolution. For some of the ETK waveforms, the gravitational wave signal is too noisy to work with the quadrupole aligned frame, due to an inappropriate configuration of the wave extraction grids. This problem and its resolution will be discussed in a separate paper. The z axis is then chosen to point in the direction of the orbital angular velocity $\vec{\omega}$,

$$\vec{\omega}(t) = \frac{\vec{r} \times \vec{v}}{r^2} = \frac{\vec{r} \times \dot{\vec{r}}}{r^2}, \tag{2.9}$$

where $\vec{r}$ is the vector that points from the smallest black hole to the largest ($\vec{r} = \vec{x_1} - \vec{x_2}$), and the x axis is chosen to point in the $\vec{r}$ direction (see Fig. 4 for visual definition). The y axis is defined as usual to complete an orthogonal right-handed triad.

In order to perform this alignment, one needs the time evolution of the two black hole positions, as well as the time evolution of all the quantities we include in our dataset. These are the spins and masses of both initial black holes and the remnant, the emitted waves, the radiated energy, and/or orbital frequencies, although additional information on how to get these quantities is recommended to ensure consistency. Some public catalogs are hence not adequate for our purposes, e.g., the RIT catalog [21] includes precessing waveforms, but it does not provide the trajectory evolution. For future work, we also plan to include the most recent MAYA catalog [24].

We adopt the same reference time for defining the spin components in a co-orbital frame as in [12,40], which is set to $100M$ before merger. This choice facilitates direct comparisons between our remnant model and NRSur7dq4EmriRemnant [40]. The binary evolution closely approaches the merger state at this reference time, thus one can expect a simpler functional dependence for the remnant quantities. For the EMR limit, the ISSO provides an approximate plunge time. For our numerical EMRI dataset detailed in Sec. II B, we compare the numerical preserved quantities at merger with those obtained at the ISSO time. For our EMRI dataset, the ISSO time ranges from $-700M$ for the most antialigned cases to $-150M$ for the aligned ones. Upon comparing the values for the preserved quantities obtained by solving the geodesic equations at the ISSO with the numerical results, we observe maximum relative errors of 0.1%. Consequently, we conclude that the ISSO time can be effectively employed as the reference time for the EMR limit without impacting the transition from the comparable mass regime, where the chosen reference time is $-100M$. These observations, however, suggest that this choice might not be optimal. Instead, a quantity that smoothly transitions from

the comparable mass reference time to the ISSO could be more suitable, such as the minimal energy circular orbit time [70]. We leave this as future work, to investigate further a choice of optimal reference time, which allows simple yet precise fits and an accurate match with fast post-Newtonian inspiral codes, e.g., [71]. These codes serve to bridge the gap between the reference time and some earlier time where waveform models define their spin vectors.

The rotation of the vector quantities such as the black holes' spins is straightforward, consisting of a fixed rotation to the full time array. For the waveforms, it is common to decompose the waves into spherical harmonics and rotate each mode individually via Wigner matrices. Comparable mass binaries are usually described at the co-orbital frame at some reference time close to the initial time, and performing a fixed rotation to a later co-orbital frame does not suppose higher complications. More efforts need to be done, however, for the extreme mass ratio limit, where the natural frame is defined in terms of the largest black hole spin. From the trajectories, one can obtain the vector $\vec{r} = -\vec{x_2}$, as in Eq. (2.6), then compute the velocity $\dot{\vec{r}}$ and finally obtain the z axis given by $\hat{\omega}(t_{\rm ref})$. In the case of using geodesics, one just inputs the inclination angle at the reference time. Once the alignment is done for all simulations, we keep the metadata at the chosen reference time $-100M$ where the alignment takes place. This includes the mass ratio, the two black holes' spins and positions, the reference orbital frequency, the time of merger, and finally the remnant quantities.

2. Extreme mass ratio limit

In the EMR limit, the final mass and spin can be computed to first order in the mass ratio from the energy and orbital angular momentum at the ISSO, since the contribution of the plunge can be neglected [72]. The quantities E and L_z are preserved for geodesics and can thus be evaluated directly for any geodesic. This is, however, not true for the full angular momentum vector, which would require further knowledge about the spacetime. According to the previous discussion around Eq. (2.5), we approximate L_ρ by the square root of the Carter constant $\sqrt{Q}$ and extract the direction of the final spin with respect to the z axis. Since only the z or the in-plane components are preserved, there will be a freedom regarding the in-plane direction of the final spin that we will not be able to fix. Regardless, here we are only interested in the final spin magnitude, so the missing direction does not constrain our work.

Numerically solving the geodesic equations detailed in Appendix A allows one to determine the constants of motion at a specific geodesic. As previously discussed, in the EMR limit, we select the ISSO time as the reference time. At this point, the conditions $R(r_{\rm ISSO}) = R'(r_{\rm ISSO}) = R''(r_{\rm ISSO}) = 0$ are satisfied [refer to Eq. (A4)]. Solving this set of algebraic equations provides the constants of motion (E, L_z, Q) at the ISSO, as well as the radius $r_{\rm ISSO}$. This numerical procedure is described in Ref. [73] and implemented in the KerrGeodesics *Mathematica* package, which we have utilized extensively to solve precessing geodesics throughout.

For the specific case of nonprecessing orbits ($I = \{0, \pi\}$), one can derive simple analytical expressions for the energy and angular momentum at the ISCO (particular ISSO for equatorial orbits), given by

$$\tilde{E}_{\rm ISCO}(\chi_f) = \sqrt{1 - \frac{2}{3\rho_{\rm ISCO}(\chi_f)}}, \tag{2.10}$$

and

$$\tilde{L}^{\rm orb}_{\rm ISCO}(\chi_f) = \frac{2\left(3\sqrt{\rho_{\rm ISCO}(\chi_f)} - 2\chi_f\right)}{\sqrt{3\rho_{\rm ISCO}(\chi_f)}}, \tag{2.11}$$

where $\rho_{\rm ISCO}$ is the radius at the ISCO,

$$\begin{aligned}\rho_{\rm ISCO}(\chi) &= 3 + Z_2 - {\rm sign}(\chi)\sqrt{(3 - Z_1)(3 + Z_1 + 2Z_2)},\\ Z_1 &= 1 + (1-\chi^2)^{1/3}\left[(1+\chi)^{1/3} + (1-\chi)^{1/3}\right],\\ Z_2 &= \sqrt{3\chi^2 + Z_1^2}.\end{aligned}$$

From these equations, it is clear that the derivative of the final mass and spin with respect to the component spin is singular at $\eta = 0$ when the black hole spin is extremal and aligned with the orbital angular momentum. For other mass ratios, this derivative is regular, as is the derivative with respect to η. This behavior is difficult to capture in models without further analytical insight in the region near the singular point where $\eta = 0$ and the component spins are extremal. Further work will be required to fully resolve the associated issues.

Approximating the orbital angular momentum magnitude L by $\sqrt{L_z^2 + Q}$, the remnant quantities in Eqs. (2.7) and (2.8) depend exclusively on the "preserved" quantities (E, L_z, Q). While the numerical dataset provides these values after the plunge, for the geodesic description we take these values from the ISSO and neglect the contribution from the plunge [72]. We scaled the radiated energy by η at linear order, which is consistent with our earlier discussion that the geodesic values are accurate up to order η. We compare the final mass and spin magnitude obtained from the precessing geodesic equations and the numerical EMRI data in Fig. 5, showing a maximum error around 10^{-6}, comparable to the numerical error expected from the simulations.

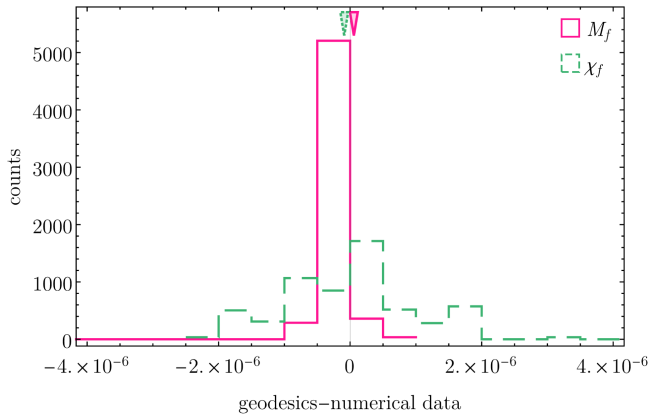

FIG. 5. Histogram illustrating the difference between the remnant properties obtained by solving the precessing geodesic equations at the ISSO and the corresponding numerical values from the used EMRI dataset described in Sec. II B. The triangles represent the median value for each distribution.

III. MODELS FOR THE REMNANT MASS AND SPIN

In this section, we develop fits for the remnant mass and spin for precessing binaries, extending some of the ideas that have been used in [36] to create such fits for aligned spin binaries. We use extreme mass ratio data and split the input parameter space (in a hierarchical way) by dimension to design a class of functional forms for the fits. We use information criteria to select the best fit among this class of functions preventing overfitting.

At high mass ratios, the contribution of the secondary spin becomes a subdominant effect. This makes the single spin subspace a natural arena when trying to understand the high mass ratio regime for precessing systems and gain intuition on how to bridge the gap to comparable mass binaries (through intermediate mass ratio systems). The problem thus becomes four dimensional, with three dimensions due to the largest black hole spin, $(\chi_1, \theta_1, \phi_1)$, and one for the symmetric mass ratio η. To assess the impact of the in-plane spin orientation ϕ_1 on the remnant quantities, we utilize the NRSur7dq4EmriRemnant model, which has been calibrated to numerical relativity and includes the ϕ_1 dimension. For all configurations in our full numerical relativity single spin dataset, we compute the residual error between the NR values for the remnant quantities and those obtained with NRSur7dq4EmriRemnant, first using the value of $\phi_1^{\rm ref}$ from the simulation and then a random value. The results, depicted in Fig. 6, reveal that the root-mean-square errors are virtually unaffected by this additional dimension and that the error distribution exhibits similar behavior. This supports the decision to exclude the ϕ_1 dimension in this study, reducing our dimensionality to three free parameters and thereby lowering the computational cost of the procedure. We leave the incorporation of the ϕ_1 dependence for future work.

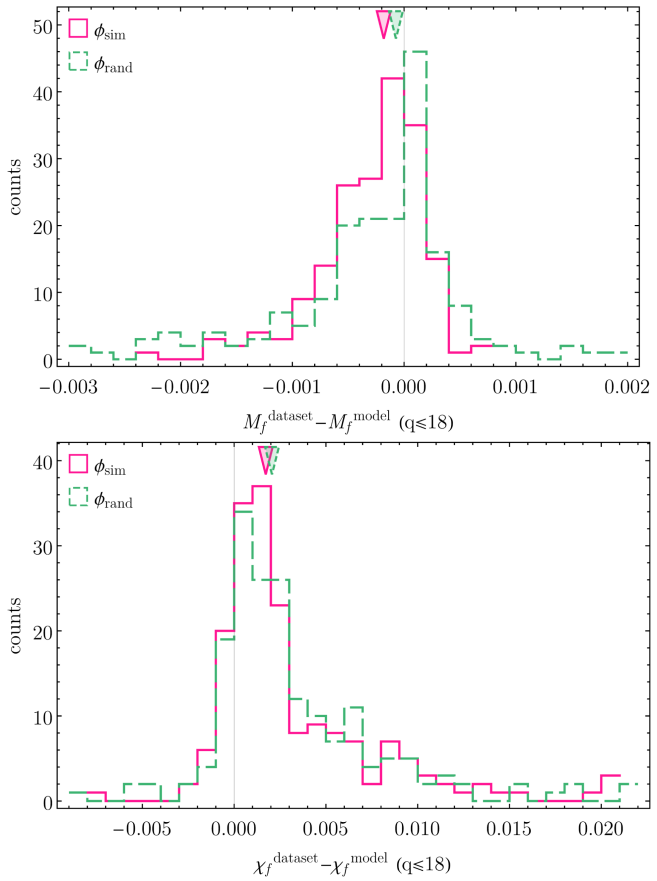

FIG. 6. Error histograms illustrating the effect of the in-plane orientation of the single spin ϕ_1 on the NRSur7dq4EmriRemnant model for the remnant properties. We consider the corresponding ϕ_1 of each simulation ($\phi_{\rm sim}$ in the legend) and a random angle value ($\phi_{\rm rand}$) and compare the error distributions for our dataset. Top: the errors associated with the final mass (with a RMSE $= 5.4 \times 10^{-4}$ for the $\phi_{\rm sim}$ distribution and RMSE $= 8.2 \times 10^{-4}$ for $\phi_{\rm rand}$). Bottom: the errors related to the final spin magnitude [RMSE$(\phi_{\rm sim}) = 5.4 \times 10^{-3}$ and RMSE$(\phi_{\rm rand}) = 5.8 \times 10^{-3}$]. Triangles indicate the median value for each distribution. Both plots suggest that ϕ_1 does not significantly influence the error distribution of the model, supporting our decision to exclude that dimension from our studies.

The twisting up procedure introduced in Sec. II C permits one to understand precession in terms of an approximate map between aligned spin binaries and precessing ones in a co-orbital frame. Our strategy will be to work in a co-orbital frame to facilitate constructing our fits as corrections to the values of the corresponding aligned spin binary configuration. The misaligned spin components induce a precessing motion of the binary, which introduces a new timescale compared to aligned spin systems. During the inspiral this precessing timescale is, however, much slower than the orbital one, so its effect on the energy radiated in gravitational waves is rather small. For the radiated angular momentum we will see that the situation is slightly more complicated: because the angular momentum

and the component spins are time-dependent vectors, the final angular momentum is affected by a nontrivial vector addition effect. For a recent discussion in the context of current waveform models see, e.g., [74].

To prevent overfitting, we follow Ref. [36], where aligned spin remnant fits were developed, and we use the Bayesian information criterion (BIC) and Akaike information criterion as metrics for model selection. These criteria are designed to balance model accuracy and complexity to avoid overfitting. For further details on the definition of the information criteria, see Appendix B. We focus in particular on the BIC, which provides a more restrictive criterion for our purposes. A lower BIC value indicates a more favorable trade-off between model fit and complexity, leading to the selection of a model with improved predictive performance.

Our input dataset consists of the single spin simulations displayed in Fig. 2. Our calibration parameter space extends only up to $\chi_1 = 0.8$. However, we discuss extrapolation to extreme spins in Appendix D, where we conclude that our model extrapolates well to maximally precessing spins.

We evaluate the accuracy of the remnant fits and compare with the results obtained with NRSur7dq4EmriRemnant, which is calibrated against double spin numerical relativity simulations, and with the remnant fits that are being used in existing precessing phenomenological models [6,7], which are only calibrated to aligned spin simulations. By subtracting information from the aligned spin sector and EMR before the fits, we can construct simple parametrized fits that provide a far higher accuracy than what is currently required for gravitational wave observations, as does the NRSur7dq4EmriRemnant model, but at a much reduced complexity and computational cost.

A. Remnant mass

Since the correction of the final mass due to precession is expected to be small when parametrizing the input spins in a co-orbital frame, it is natural to directly fit the effect of precession on the aligned spin radiated energy. We then define our fitting quantity as

$$\Delta E = E_{\rm rad}^{\rm prec}(\eta,\chi_1,\theta_1) - E_{\rm rad}^{\rm AS}(\eta,\chi_1\cos(\theta_1),\chi_2\cos(\theta_2)=0), \tag{3.1}$$

so the final mass of a precessing binary will be modified as

$$M_f = 1 - E_{\rm rad} = 1 - \Big(E_{\rm rad}^{\rm AS}(\eta,\chi_1\cos(\theta_1)) + \Delta E(\eta,\chi_1,\theta_1)\Big), \tag{3.2}$$

where all the input parameters are taken at the reference time. Since by design our fitted quantity ΔE has very small values, we need to ensure that poor accuracy of the aligned spin fit for the energy does not contaminate our error budget. What we found is that the previous fit developed in Ref. [36] did not accurately capture the radiated energy close to the joint extremal spins and extreme mass ratio limit. Hence, we first improved the aligned spin fit near this singular point as shown in Fig. 7, where we defined $\Delta E_{\rm rad}^{\rm AS}$ as the difference between the updated fit and the old one. The updated expression is provided in Appendix C, Eq. (C2), and will be discussed in detail elsewhere.

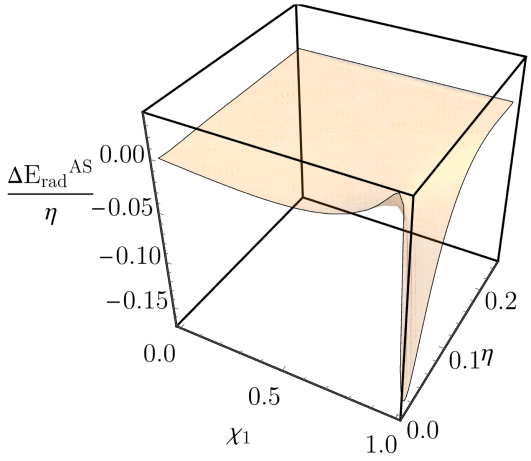

FIG. 7. Difference between the updated aligned spin fit for the radiated energy [see Eq. (C2)] and the previous one [36] used in phenomenological families IMRPhenomX [34] and IMRPhenomT [35] for single spin systems, scaled by the mass ratio. The key enhancement in the new model is a more accurate description of the singularity at $\chi_1 \to 1$ and $\eta \to 0$.

In order to improve the conditioning of our fitting method for the EMRI regime we use the geodesic results, which are valid at linear order in η: We subtract the resulting linear-in-η term from the numerical dataset and only include higher powers of η in our fits. Figure 8 shows that the linear-in-η term is small for comparable masses, which benefits this strategy by not contributing much where the linear approximation is not valid. We therefore fit the quantity $\overline{\Delta E}$ defined as

$$\overline{\Delta E} = \Delta E - \Delta E_{\rm EMR}. \tag{3.3}$$

Here $\Delta E_{\rm EMR}$ is computed using the KerrGeodesics *Mathematica* package for the energy in the precessing case and Eq. (2.10) for the aligned spin energy case.

In order to develop a suitable *Ansatz* for a parametric fit across the three-dimensional space (η,χ_1,θ_1), we first visualize only two dimensions and show results for fixed values of θ_1, chosen as the evenly spaced grid points of the BAM catalog [23]: $\theta_1 \in \{\frac{\pi}{6},\frac{\pi}{3},\frac{\pi}{2},\frac{2\pi}{3},\frac{5\pi}{6}\}$. This way, we ensure that each fitted surface contains numerical relativity data. By definition, $\overline{\Delta E}$ (as well as ΔE) has to vanish at the boundaries $\theta_1 \in \{0,\pi\}$, so that we recover the aligned and antialigned limits. The simple structure of the numerical values of ΔE (and hence $\overline{\Delta E}$) across the $\eta - \chi_1$ subspace at

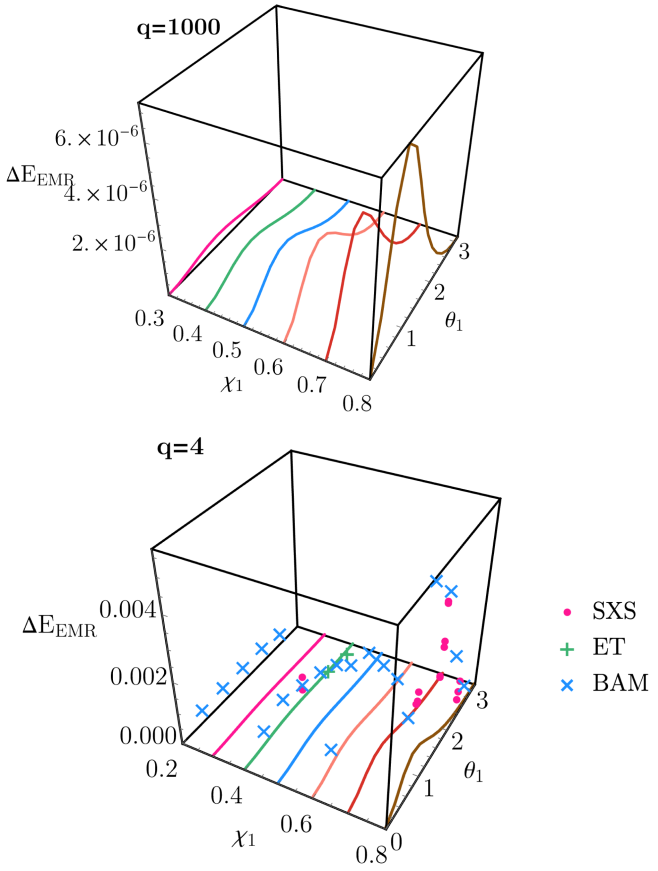

FIG. 8. Numerical evaluations of ΔE as defined in Eq. (3.1) for the extreme mass ratio limit (denoted as $\Delta E_{\rm EMR}$) at a fixed mass ratio while varying the black hole's spin magnitude χ_1 and its orientation with respect to the orbital frequency at the reference time θ_1. The precessing and aligned spin radiated energies are obtained from the geodesic equations of motion, which provide the linear contribution in η to the energy. The precessing radiated energy at the ISSO is obtained with the KerrGeodesics package, whereas the aligned spin energy is computed from Eq. (2.10). Top: corresponds to a mass ratio of 1000, where the geodesic equations are expected to be valid. Bottom: corresponds to a mass ratio of 4. In the lower plot, we included the single spin simulations from Fig. 2 that fall into this subspace.

the fixed values of θ_1 (see, e.g., Fig. 10) suggests that a simple polynomial *Ansatz* can effectively capture its behavior. More specifically, our *Ansatz* consists of $\eta^a\chi_1^b$-like terms using a rectangular grid in (a,b). Visually inspecting the data, the highest order fit that avoids overfitting for any fixed θ_1 is given by $a \leq 5$ and $b \leq 2$, which results in 18 terms in the polynomial *Ansatz*. However, many of these terms can be discarded.

We set the constant term ($a = b = 0$) of the expansion to 0 because, at $\chi_1 = 0$ and $\eta \to 0$, it holds that $\overline{\Delta E} = 0$, leaving us with 17 terms. These data points with corrections set to zero are designated as AS, since one recovers the underlying aligned spin model. We utilize the LinearModelFit function from *Mathematica* [75] to fit the numerical data for each θ_1 surface and record the BIC of the resulting model across all θ_1's. Subsequently, we perform a weighted averaging of the BIC for each surface, assigning weights of 0.05 for $\theta_1 \in \{\frac{\pi}{6}, \frac{5\pi}{6}\}$, of 0.2 for $\theta_1 \in \{\frac{\pi}{3}, \frac{2\pi}{3}\}$, and finally, 0.5 for $\theta_1 = \frac{\pi}{2}$. The assignment of weights depends on the nature of the quantity being fitted: the magnitude is more significant for highly precessing systems, making the results more reliable in the region closer to in-plane spins ($\theta_1 \sim \pi/2$). Conversely, for systems close to aligned or antialigned configurations, the value is so small that it is overshadowed by the numerical error of the simulations. By employing weighted averaging, we ensure that the fitting procedure is not dominated by the numerical errors in our dataset, while still taking into account all cases. This process is repeated iteratively for a modified *Ansatz* where each term is removed, saving the averaged BIC for each case. We retain the *Ansatz* with the lowest mean BIC only if it falls below the BIC value of the initial polynomial set. This procedure is reiterated until removing more terms no longer contributes positively to the final fit. With this procedure, we obtain a final fit with only seven terms favored by about −44 in relative BIC. Then, for every value of $\theta_1 \in \{\frac{\pi}{6}, \frac{\pi}{3}, \frac{\pi}{2}, \frac{2\pi}{3}, \frac{5\pi}{6}\}$, we have

$$\{a_i\}_{i=1}^{i=7}(\eta^2\chi_1, \eta^3\chi_1, \eta^3\chi_1^2, \eta^4\chi_1, \eta^4\chi_1^2, \eta^5\chi_1, \eta^5\chi_1^2). \quad (3.4)$$

Upon visually inspecting each a_i, we observed that the contribution of the $\eta^2\chi_1$ term was minimal, supporting its removal from the final fit. Consequently, we are left with six coefficients to fit for θ_1. Thereafter, we proceed to fitting the θ_1 dependence of the coefficients a_i. As previously mentioned, at the boundaries $\theta_1 \in \{0, \pi\}$, we recover the aligned and antialigned limits, implying that $a_i(0) = a_i(\pi) = 0$. Given that θ_1 is an angle, it makes sense to propose a sinusoidal *Ansatz* such as

$$a_i(\theta_1) = A_i \sin\theta_1 + B_i \sin 2\theta_1, \quad (3.5)$$

which will always satisfy the boundary conditions. Figure 9 shows the functional dependence of the $\eta^3\chi_1$ term in θ_1 and the corresponding fit from the above *Ansatz* in Eq. (3.5).

The final expression for $\overline{\Delta E}(\eta, \chi_1, \theta_1)$ is given by

$$\begin{aligned}\overline{\Delta E}(\eta,\chi_1,\theta_1) = {}& \eta^3\chi_1[0.759123\sin(\theta_1) - 2.33392\sin(2\theta_1)] \\ & + \eta^3\chi_1^2[6.51059\sin(\theta_1) + 7.06906\sin(2\theta_1)] \\ & + \eta^4\chi_1[-11.7873\sin(\theta_1) + 22.364\sin(2\theta_1)] \\ & + \eta^4\chi_1^2[-37.0594\sin(\theta_1) - 63.3841\sin(2\theta_1)] \\ & + \eta^5\chi_1[35.0427\sin(\theta_1) - 51.36\sin(2\theta_1)] \\ & + \eta^4\chi_1^2[-37.0594\sin(\theta_1) - 63.3841\sin(2\theta_1)]. \end{aligned} \quad (3.6)$$

Figure 10 shows ΔE computed as in Eq. (3.3) together with the numerical values for the entire dataset at $\theta_1 = \pi/2$.

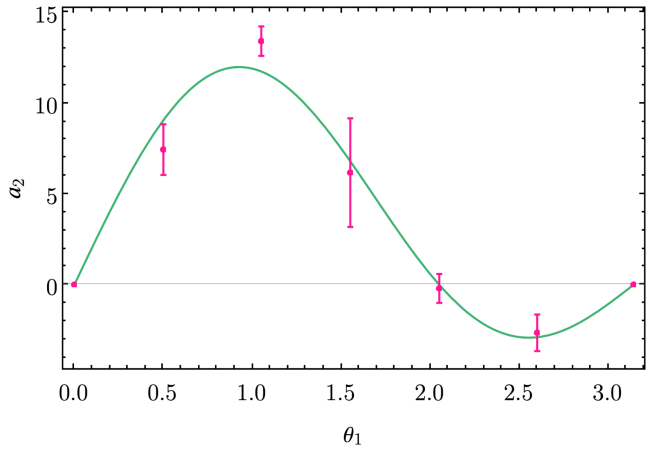

FIG. 9. Functional dependence of the $\eta^3\chi_1$ term on the angle θ_1 [following the *Ansatz* given by Eq. (3.5)], as depicted in Eq. (3.6). Similar results are obtained for the remaining five terms of the parametrized fit for $\overline{\Delta E}$. All fits were performed with the FIT function in *Mathematica* [76].

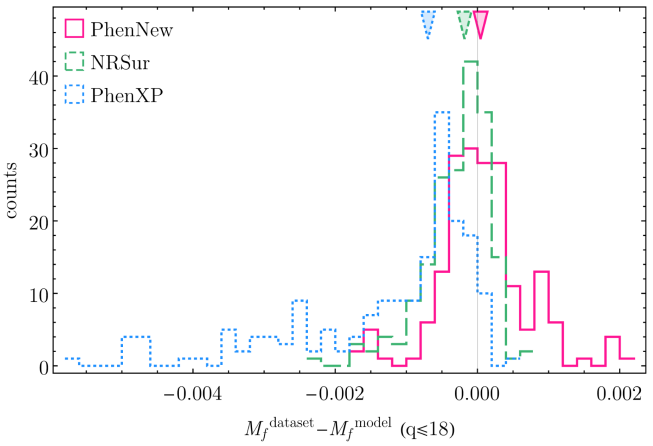

FIG. 11. Histogram of the errors in the remnant mass computed with each of the three models for our single spin precessing dataset presented in Fig. 2. The model developed in this project is labeled as PhenNew, the underlying model as PhenXP, and NRSur7dq4EmriRemnant as NRSur. The triangles above the distributions represent their median values, also included in Table II. This table provides additional information on the distributions: the computational time needed to evaluate the dataset for each model, along with the RMSEs. Note that the PhenXP model shows a sensible bias that is significantly reduced in the PhenNew model.

This fit can now be inserted into Eq. (3.2) in order to get the new model for the mass of the remnant object. To compute the final mass of the corresponding aligned system, we rely on the updated IMRPhenomX model given by Eq. (C2).

We can now assess the accuracy of our new model. For the entire single spin precessing dataset, we calculate the final mass using our model [Eqs. (3.2) and (3.6)], denoted as PhenNew. We compare this with the current IMRPhenomX model, which does not account for the ΔE correction (PhenXP), and with NRSur7dq4EmriRemnant for validation. Figure 11 presents the histogram of errors

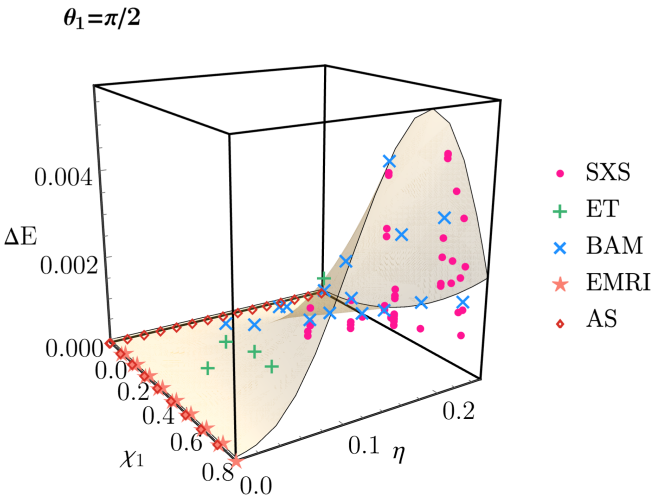

FIG. 10. Numerical evaluation of ΔE as defined in Eq. (3.1), obtained from the parametrized fit $\overline{\Delta E}$ (3.6) and ΔE_{EMR}, at a fixed spin orientation $\theta_1 = \pi/2$, while varying the mass ratio η and the spin magnitude χ_1. The figure includes the single spin precessing simulations shown in Fig. 2 that fall into this subspace, as well as the vanishing corrections for the limits $\eta \to 0$ and $\chi_1 = 0$, denoted as AS.

associated with each model. Results are based on the NR data from our dataset, comprising 184 simulations with $q \leq 18$. The EMRI dataset has been excluded from the comparison due to its large number of simulations and small errors. Table II provides the computational time required to evaluate the final masses and spins for the whole NR dataset, along with the numerical values of the median error and root-mean-square error (RMSE) computed as in Eq. (B1). The PhenXP model for the final mass M_f involves evaluating the aligned spin model for the radiated energy using Eq. (C2). On the other hand, PhenNew evaluates both Eq. (C2) and the parametrized fit for $\overline{\Delta E}$ (3.6), as well as ΔE_{EMR}, using the KerrGeodesics package. Note that computational times refer to a straightforward implementation in *Mathematica*, with most of the computational time required to solve the precessing geodesic equations to obtain ΔE_{EMR}. An optimized implementation and a fit to the analytically known EMR results would dramatically accelerate the evaluation. For the evaluation of the NRSur model, we utilized the SurfinBH PYTHON package [12] with the NRSur7dq4EmriRemnant [40] model. In this case, the evaluation time is provided as a single number for both the final mass and spin because both are returned together as an array. It takes approximately 5 ms to compute the remnant properties for one binary black hole configuration, consistent with the findings in [40]. It is noteworthy that NRSur7dq4EmriRemnant incorporates the direction of the final spin, thereby introducing complexity to the model which is reflected in the computational time.

TABLE II. Median value and RMSE of the error distributions of the remnant mass M_f and spin magnitude χ_f for different models, with respect to the numerical relativity dataset shown in Fig. 2. The histograms of the distributions are shown in Figs. 11 and 15, respectively. The last row provides the averaged time (Av. ev. time) needed to evaluate the complete dataset (184 simulations) with each model for the final mass/final spin. For the NRSur7dq4EmriRemnant model (NRSur) only one value is provided because their PYTHON implementation jointly returns both quantities.

		PhenNew	PhenXP	NRSur
M_f	Median	4.4×10^{-5}	-7.0×10^{-4}	-1.8×10^{-4}
	RMSE	6.4×10^{-4}	1.8×10^{-3}	5.4×10^{-4}
χ_f	Median	1.5×10^{-4}	-8.6×10^{-3}	1.7×10^{-3}
	RMSE	3.4×10^{-3}	1.5×10^{-2}	5.4×10^{-3}
Av. ev. time (ms)		0.55/2.7	0.019/0.071	5.2

These findings demonstrate that our new model for the final mass achieves an accuracy comparable to the NRSur7dq4 model, surpassing the original PhenXP model, while maintaining its computational efficiency. Additionally, PhenNew exhibits a less biased error distribution compared to the old model, which tends to overestimate the final mass.

To ensure completeness, we assessed the resulting model beyond our calibration region, specifically when $\chi_1 > 0.8$. We focused on scenarios where precession effects are maximal, corresponding to an in-plane spin configuration, i.e., $\theta_1 = \pi/2$. We include the result of the extrapolation in Appendix D. Despite the absence of numerical data in that region, the study indicates that the extrapolation behaves well, and no dubious features emerge outside the calibration regime.

B. Remnant spin

If one assumes the twisting-up approximation and that the in-plane and aligned spin components are conserved, then one can write the final spin magnitude as

$$\chi_f^{\rm prec} = \sqrt{\chi_f^{\rm AS^2} + \frac{m_1^4}{M_f^4}\chi_\perp^2}, \tag{3.7}$$

where $\chi_\perp$ is the total in-plane spin. Variants of this approximation with different assumptions to compute $\chi_\perp$ have been used in the IMRPhenomX and IMRPhenomT waveform models [6,7]. In our case, considering only the single spin sector, $\chi_\perp$ simply becomes the in-plane component of the larger black hole. However, the in-plane and orthogonal spin components are not exactly conserved, and we therefore introduce a correction term δ^2 that we fit to our numerical dataset. Note that denoting the unknown quantity as δ^2 is an abuse of notation, since it is not necessarily positive and indeed typically is negative. Consequently, the final spin of a precessing system can be written as

$$\chi_f^{\rm prec} = \sqrt{\chi_f^{\rm AS^2} + \frac{m_1^4}{M_f^4}\chi_\perp^2 + \delta^2}, \tag{3.8}$$

where $\chi_1^\perp$ in the single spin case is given by $\chi_1^\perp = \chi_1 \sin(\theta_1)$, and $M_f = 1 - E_{\rm rad}$, where we use the model of the previous section to compute $E_{\rm rad}$.

One can develop the previous equation and turn it into a closed-form approximation for the extreme mass ratio limit by using Eq. (2.8) for both the precessing and aligned final spin, assuming that the Carter constant is approximately the in-plane orbital angular momentum ($Q \approx L_\rho^2$). This procedure results in

$$\delta^2_{\rm EMR} = \frac{M^4}{M_f^4}\left[\frac{m_2^2}{m_1^2}\left(\tilde{L_z}^2 + \tilde{Q} - \tilde{L_z^\parallel}\right) + 2\frac{m_2}{m_1}\chi_1\cos(\theta_1)\left(\sqrt{\tilde{L_z}^2 + \tilde{Q}} - \tilde{L_z^\parallel}\right)\right]. \tag{3.9}$$

The main advantage of this expression lies in the fact that it relies exclusively on geodesic information for precessing and aligned equations. Remarkably, even for close to comparable masses, its behavior closely resembles that obtained from numerical data, up to a scaling factor, as can be seen in the lower panel of Fig. 12. Equation (3.9) consists of two contributions: the first term, quadratic in $1/q$, and the second term, linear. Both terms are shown in Fig. 12. The linear term dominates for extreme mass ratios (in dotted lines, covered by the continuous lines) and exhibits oscillations due to the cosine dependence of the inclination angle. However, as the mass ratio increases, these oscillations are overshadowed by the growth of the quadratic contribution (depicted by dashed lines), as shown in the lower panel of Fig. 12. It turns out that, in order to reproduce our numerical data in the comparable mass regime, it is best to keep both the linear and quadratic in η terms. Following the same motivation as for the energy, we proceed to subtract $\delta^2_{\rm EMR}$ from our fitting quantity δ^2 to capture the EMRI regime, defining

$$\overline{\delta^2} = \delta^2 - \delta^2_{\rm EMR}, \tag{3.10}$$

where again $\delta^2_{\rm EMR}$ is computed using the KerrGeodesics *Mathematica* package.

The fitting procedure then follows the same structure described in the previous subsection. We first compute δ^2 from Eq. (3.8) for all the single spin simulations in our precessing dataset. We again neglect the in-plane spin angle ϕ_1, reducing our independent variables to (q, χ_1, θ_1). We then show $\overline{\delta^2}$ for fixed values of θ_1, chosen to be the same values as for the energy: $\theta_1 \in \{\frac{\pi}{6}, \frac{\pi}{3}, \frac{\pi}{2}, \frac{2\pi}{3}, \frac{5\pi}{6}\}$. Again, at

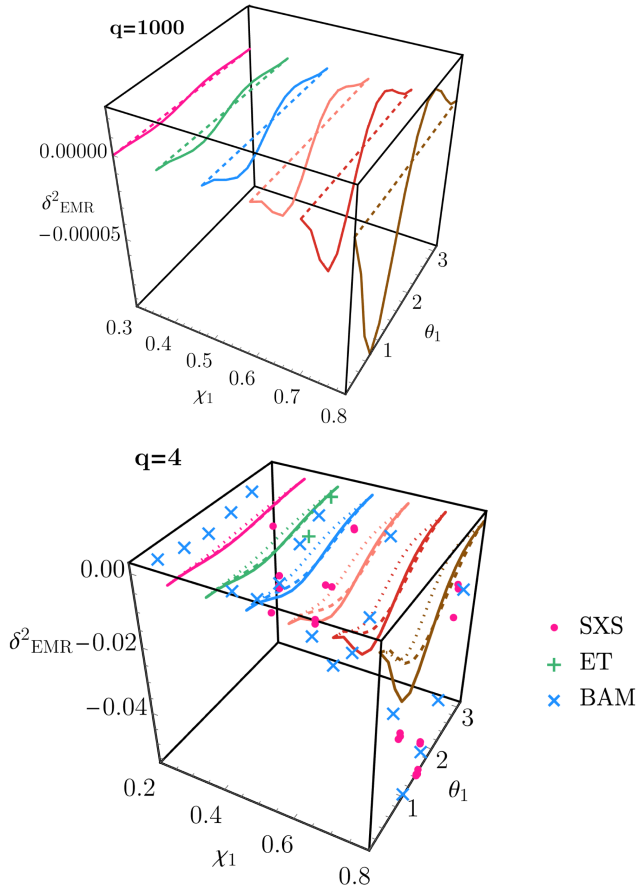

FIG. 12. Numerical evaluation of $\delta^2_{\rm EMR}$ as defined in Eq. (3.9). The constants of motion L_z, Q, and E are obtained from the precessing geodesic equations, while $L_z^{\parallel}$ is computed from Eq. (2.11). Dotted lines show the linear term in Eq. (3.9) and dashed lines, the quadratic term. We solve the precessing geodesic equations at the ISSO using the KerrGeodesics package at a fixed mass ratio, while varying the black hole's spin magnitude χ_1 and its orientation with respect to the orbital frequency at the reference time θ_1. Top: corresponds to a mass ratio of 1000, where the geodesic equations are expected to be valid. Bottom: corresponds to a mass ratio of 4, where they are expected to fail. In the lower plot, we included the single spin simulations from Fig. 2 that fall into this subspace.

$\theta_1 \in \{0, \pi\}$, δ^2 is defined to vanish so one recovers the nonprecessing limit. In order to find an appropriate *Ansatz* in this case, we start our procedure with $a \leq 3$ and $b \leq 2$. We then followed the iterative procedure described above to reduce our grid from 11 to 7 coefficients, representing an improvement of −16.5 in BIC. Then, for every fixed value of θ_1, we have

$$\{a_i\}_{i=1}^{i=7}(\chi_1^2, \eta\chi_1, \eta\chi_1^2, \eta^2\chi_1, \eta^2\chi_1^2, \eta^3\chi_1, \eta^3\chi_1^2). \tag{3.11}$$

Finally, five more coefficients can be discarded when inspecting their θ_1 dependence, resulting in a very simple *Ansatz* for $\overline{\delta^2}$,

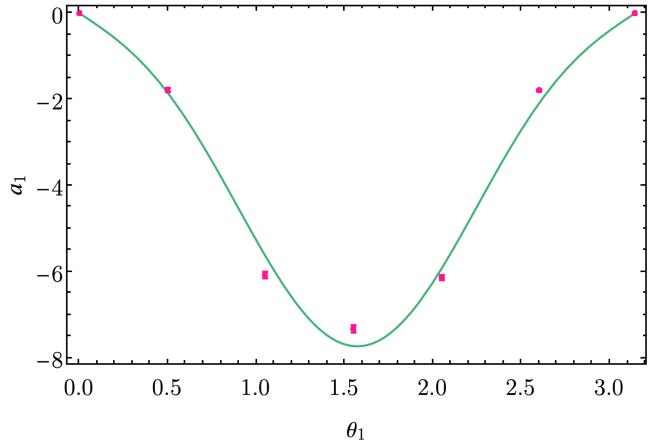

FIG. 13. Functional dependence of the $\eta^2\chi_1^2$ term on θ_1 [following the *Ansatz* given by Eq. (3.13)], as depicted in Eq. (3.14). Similar results are obtained for the remaining term of the parametrized fit for $\overline{\delta^2}$. All fits were performed with the FIT function in *Mathematica* [76].

$$\{a_i\}_{i=1}^{i=2}(\eta^2\chi_1^2, \eta^3\chi_1^2). \tag{3.12}$$

We propose again a sinusoidal *Ansatz* for the coefficients a_i which satisfies the boundary conditions

$$a_i(\theta_1) = A_i \sin\theta_1 + B_i \sin 3\theta_1. \tag{3.13}$$

Figure 13 shows an example of the functional dependence of the first fit coefficient a_1 ($\eta^3\chi_1^2$) in terms of θ_1.

The resulting fit is finally given by

$$\begin{aligned}\overline{\delta^2}(\eta, \chi_1, \theta_1) = {} & \eta^2\chi_1^2[1.25552\sin(3\theta_1) - 6.47984\sin(\theta_1)] \\ & + \eta^3\chi_1^2[27.0456\sin(\theta_1) - 4.71194\sin(3\theta_1)],\end{aligned} \tag{3.14}$$

and it is represented in Fig. 14 for $\theta_1 = \pi/2$, together with the numerical δ^2 values for the entire dataset. Note that the plot shows δ^2, which is computed from Eq. (3.10). This fit can now be inserted into Eq. (3.8) in order to get the new model for the remnant spin. In this expression, the aligned spin final spin dependence goes as $\chi_f^{\rm AS}(\eta, \chi_1\cos(\theta_1))$ and the final mass is computed using the fit for $M_f(\eta, \chi_1, \theta_1)$ shown in Eq. (3.2).

We can now assess the accuracy of our new model computing the final spin for our dataset using our new model, denoted as PhenNew. We then compare it with the current IMRPhenomX model, which ignores the δ^2 correction (PhenXP) and the NRSur7dq4EmriRemnant model. Figure 15 displays the error histogram for each model relative to the numerical values, equivalent to the approach in Fig. 11, utilizing the full dataset without the EMRI waveforms. Table II provides the median and root-mean-square errors, computed as in Eq. (B1), of the

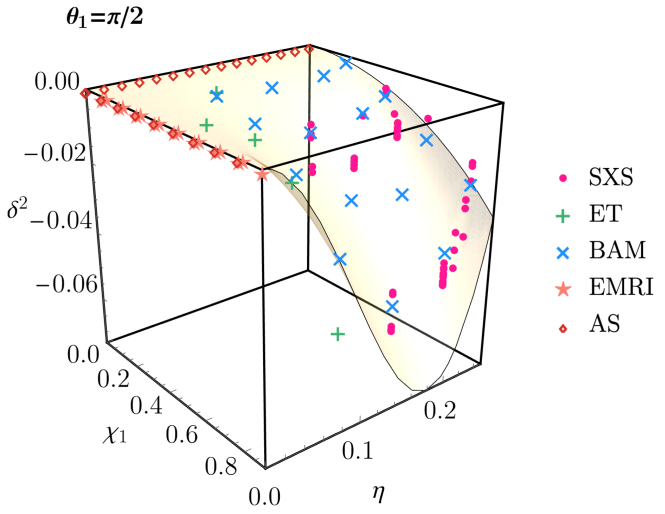

FIG. 14. Numerical evaluation of the parametrized fit of δ^2 as defined in Eq. (3.8), obtained from the parametrized fit $\overline{\delta^2}$ (3.14) and $\delta^2_{\rm EMR}$ at a fixed spin orientation $\theta_1 = \pi/2$, while varying the mass ratio η and the spin magnitude χ_1. The figure includes the single spin precessing simulations shown in Fig. 2 that fall into this subspace, as well as the vanishing corrections for the limits $\eta \to 0$ and $\chi_1 = 0$, denoted as AS.

distributions, along with the computational time required for each model evaluation. The PhenXP model for the final spin χ_f involves evaluating Eq. (3.8) assuming $\delta^2 = 0$. On the other hand, PhenNew evaluates Eq. (3.8) and the parametrized fit for $\overline{\delta^2}$ (3.14), as well as $\delta^2_{\rm EMR}$, using the KerrGeodesics package. Both models are fully assessed in

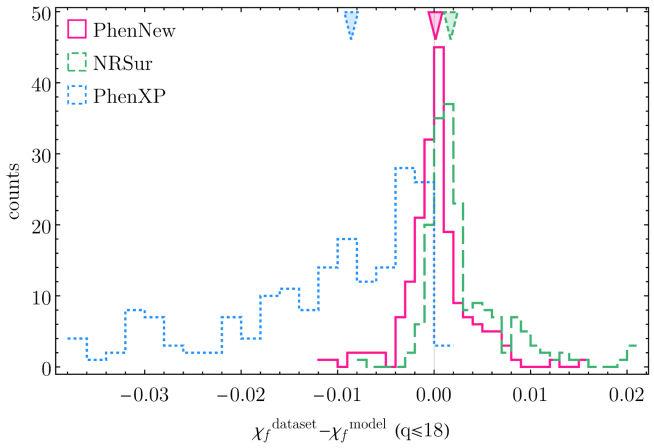

FIG. 15. Histogram of the errors in the remnant spin computed with each of the three models for our single spin precessing dataset presented in Fig. 2. The model developed in this project is labeled as PhenNew, the underlying model as PhenXP, and NRSur7dq4EmriRemnant as NRSur. The triangles represent the median of each distribution, also included in Table II. This table provides additional information on the distributions: the computational time needed to evaluate the dataset for each model, along with the RMSEs.

Mathematica, with most of the computational time attributed to solving the precessing geodesic equations to obtain $\delta^2_{\rm EMR}$. In the case of NRSur, as previously mentioned, we evaluated the NRSur7dq4EmriRemnant using the SurfinBH package, extracting the final mass and spin from the package's output. Regarding computational times, it is important to note that the provided times are for the purpose of comparison and not aimed at optimizing the code's efficiency. In the case of the model developed in this project, the majority of the evaluation time is dedicated to solving the geodesic equations. As part of future work, we anticipate parametrizing $\Delta E_{\rm EMR}$ and $\delta^2_{\rm EMR}$ to make the fits entirely parametric. The conclusions drawn from these results parallel those from the final mass: the new model offers a more accurate and less biased distribution than IMRPhenomX, achieving precision comparable to that of the NRSur7dq4EmriRemnant model while retaining the simplicity and efficiency of the model on which it is based.

To ensure completeness, we perform a final check on the extrapolation of this new remnant spin model for extreme spins (see Appendix D). Once again, we confirm that our model is well behaved even for extreme spins, despite not being calibrated in that regime, and it maintains the Kerr limit $|\chi_1| \leq 1$.

C. Cross-validation of the remnant model

In this last section, we provide additional tests of our complete remnant model. First, we compute "out-of-sample" errors to evaluate the consistency of our proposed *Ansätze*. Finally, we test the performance of our model on the entire precessing dataset, including both double and single spin simulations.

The parametrized fits shown in Figs. 10 and 14 were obtained from our single spin precessing dataset (184 simulations), yielding the in-sample errors detailed in Table II. To examine the consistency of our method, we now compute out-of-sample errors using a procedure that involves dividing the data into 23 sets of 8 random samples each. For each set, we construct the final mass and spin magnitude fits using the remaining 176 data points and test their performance against the eight validation samples. The resulting root-mean-square error values display the following mean values over the 23 sets: $\overline{\rm RMSE}(M_f) = 6.3 \times 10^{-4}$ and $\overline{\rm RMSE}(\chi_f) = 3.2 \times 10^{-3}$. These values closely match those shown in Table II, where no samples were taken to compute the fits. Therefore, we conclude that, as expected from our analysis based on information criteria, our models do not exhibit overfitting tendencies, affirming the consistency of our fitting procedure.

As a final test, we evaluate our remnant model for the complete precessing dataset outlined in Sec. II A. Although the model has been calibrated for the single spin limit, one might be interested in its performance across the full precessing quasicircular space, as well as its comparison with the currently available remnant models. Figures 11

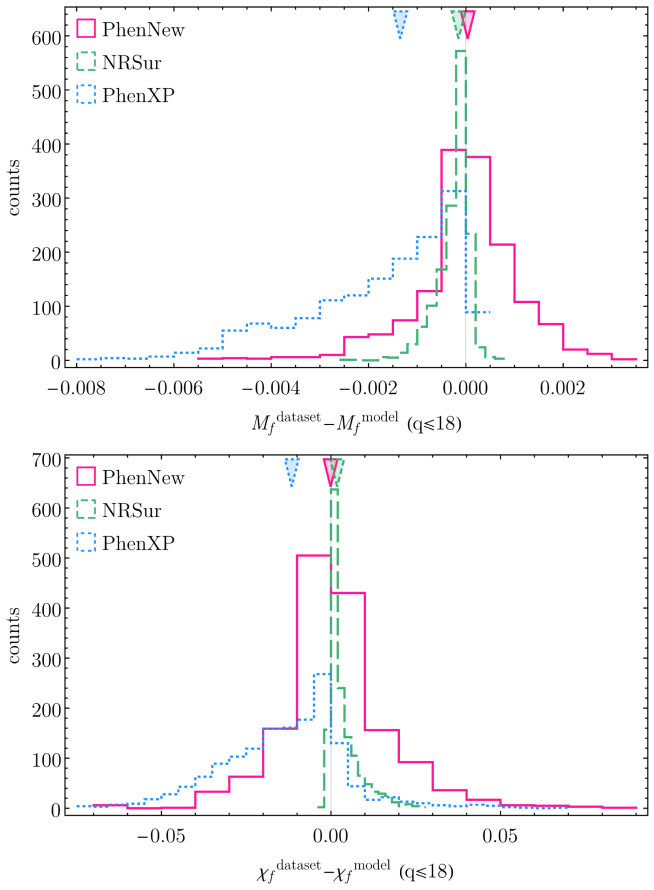

FIG. 16. Histograms of the errors in the remnant properties with each of the three models for our full precessing dataset presented in Fig. 1. PhenNew corresponds to PhenXP plus the corrections derived in Secs. III A and III B for the final mass (top) and final spin (bottom), respectively, and NRSur corresponds to the NRSur7dq4EmriRemnant model. The triangles represent the median of each distribution. Table III provides the medians along with the RMSEs for each distribution.

and 15 reveal that PhenXP exhibits a biased distribution for both the final mass and spin magnitude, tending to overestimate the real value. The fitting quantities ΔE and δ^2 consistently show a clear tendency in their sign, as evident in Figs. 10 and 14. These quantities appear as a small correction to the PhenXP model, which works for the double spin case, and hence the effect of our parametrized fits results in a slight shift toward the correct values. However, since they only account for the single spin, substantial improvements in accuracy are not expected in this scenario.

Figure 16 and Table III demonstrate that the error distributions obtained with PhenNew for the complete precessing dataset exhibit less bias compared to those obtained with PhenXP. However, given that PhenNew only considers the single spin correction, the overall performance does not exhibit a substantial improvement, as anticipated. Incorporating the double spin correction remains a direction for future work. In Fig. 16, we observed a slightly biased error distribution of the remnant properties

TABLE III. Median value and RMSE of the error distributions of the remnant mass M_f and spin magnitude χ_f for different models, with respect to the full numerical relativity dataset shown in Fig. 1. The histograms of the distributions are shown in Fig. 16, top and bottom panels, respectively.

		PhenNew	PhenXP	NRSur
M_f	Median	3.7×10^{-5}	-1.3×10^{-3}	-1.5×10^{-4}
	RMSE	1.1×10^{-3}	2.3×10^{-3}	4.2×10^{-4}
χ_f	Median	-9.9×10^{-5}	-1.2×10^{-2}	1.8×10^{-3}
	RMSE	1.6×10^{-2}	2.2×10^{-2}	6.1×10^{-3}

for NRSur7dq4EmriRemnant. Despite extensive tests, including waveform alignment using quadrupole alignment and different rotation methods, the small magnitude of the bias (see Table III) makes it challenging to track down the source of the error. Moreover, Ref. [40] only provides absolute errors, which limits further comparisons on the relative error distributions found. While it would be interesting to further understand this issue, it is not within the scope of this project, and further exploration remains a topic for future work.

IV. CONCLUSIONS

In this work, we presented a new parametrized remnant model for single spin precessing black hole binary systems at any mass ratio. We employed information from precessing geodesics at the ISSO to estimate the remnant properties in the extreme mass ratio regime and numerical data at mass ratio 1000 as a cross-check. For the final mass we have fixed the term linear in symmetric mass ratio η to the values obtained from the EMR limit, and for the final spin we have fixed both the linear and quadratic terms in η terms this way. As has become customary before, we have worked in a co-orbital frame, which drastically reduces differences between the aligned spin and precessing sectors, and in addition we have subtracted previous aligned spin fits from our data before performing the fit to the precessing dataset. These procedures have allowed us to obtain rather accurate but simple fits from a relatively small number of numerical relativity waveforms across the entire range of mass ratios. Overfitting was controlled by model selection based on the BIC information criterion and cross-checked by performing out-of-sample errors tests which confirm the consistency of our remnant models, yielding RMSEs very close to those obtained for the model utilizing the full dataset.

We observe that the correction terms that map aligned spin results to the precessing case have a dominant sign. In consequence, our models remove biases that had been present in previous simple fits that only used aligned spin numerical relativity data and are being used in precessing phenomenological waveform models [6,7]. These biases have been found to be related to the typical positive sign in

ΔE and negative in δ^2, leading to an overestimation trend in the underlying model.

The assessment of the resulting models is summarized in Table II. Our new model PhenNew surpasses its underlying baseline PhenXP used in current phenomenological models, achieving a performance akin to NRSur7dq4EmriRemnant (NRSur) at much smaller computational cost. The largest contribution to the computational cost is the evaluation of the final mass and spin contributions of the geodesic approximation. While our straightforward *Mathematica* code could be optimized, or implemented in other languages, a further path to accelerating the evaluation would be to make a fast approximate model of the geodesic contribution. The evaluation of our fits on the complete precessing dataset reveals that the new model, PhenNew, exhibits a less biased distribution compared to PhenXP, but, not surprisingly, lacks a significant overall improvement for the double spin case. In order to develop a general model of precessing remnant mass and spin, the next steps will therefore be to extend our work to the double spin case and also to include the dependency on the in-plane spin angles. In the double spin case, one faces a significantly larger parameter space (two spin vectors instead of one) and more complex phenomenology. One complication is that since the two spins will, in general, rotate at different rates, whether spins add up or cancel changes over time. This will require additional numerical relativity simulations. For our modeling approach and, in general, to better understand the phenomenology, it will be useful to have a significant number of numerical relativity simulations, where one parameter is changed at a time. One would expect that these simulations can primarily focus on the comparable mass regime, if sufficient perturbative information is available. The secondary spin is expected to function primarily as a correction to the single spin limit in scenarios involving high mass ratios, but in order to correctly model the transition from comparable to extreme mass ratios, we expect that, again, perturbative information will be essential.

In Sec. II we have discussed the problem of creating a consistent precessing dataset from several different numerical relativity catalogs. Here we have only used this heterogeneous dataset for models of the final state, using a reference time of $100M$ before the merger to define the input data for our fits to facilitate comparisons with NRSur7dq4EmriRemnant [40]. Future work should investigate the optimization of trade-offs related to the choice of reference time: later times minimize the spin dynamics between input parameters and results, whereas earlier times benefit the connection of the final state fits with models for the inspiral. Furthermore, ambiguities arise in the definition of the merger time across different datasets and in the choice of co-orbital frame. Future work will investigate these issues further. We have also created consistent datasets for the waveforms, which we have not discussed or used in this paper. This dataset is intended for the calibration of precessing waveform models to numerical relativity, where a large number of waveforms is required, and the pooling of data from different numerical relativity catalogs will be advantageous.

This work makes use of the Black Hole Perturbation Toolkit [61], in concrete, the KerrGeodesics package.

ACKNOWLEDGMENTS

We would like to thank Scott A. Hughes, Anuj Apte, Gaurav Khanna, and Halston Lim for providing the EMRI waveforms used in this project; Maite Mateu-Lucena for being involved in early stages of producing the dataset; Isabel Suárez-Fernández for running some of the Einstein Toolkit simulations; and Anna Heffernan, Antoni Ramos-Buades, Cecilio García-Quirós, and Vijay Varma for useful comments and discussions. The authors thankfully acknowledge the computer resources at MareNostrum and the technical support provided by Barcelona Supercomputing Center (BSC) through funding from the Red Española de Supercomputación (RES). M. d. L. P. is supported by the Spanish Ministry of Universities via an FPU Doctoral Grant (FPU20/05577). J. L.-Q. is supported by the Comunitat Autònoma de les Illes Balears through the Direcció General de Recerca, Innovació i Transformació Digital via an FPI Doctoral Grant No. FPI_093_2022. This work was supported by the Universitat de les Illes Balears (UIB); the Spanish Agencia Estatal de Investigación Grants No. PID2022-138626NB-I00, No. RED2022-134204-E, No. RED2022-134411-T, funded by MICIU/AEI/10.13039/501100011033 and by ESF Investing in your future; the MICIU with funding from the European Union NextGenerationEU/PRTR (PRTR-C17.I1); Comunitat Autonòma de les Illes Balears through the Direcció General de Recerca, Innovació I Transformació Digital with funds from the Tourist Stay Tax Law (PDR2020/11—ITS2017-006), the Conselleria d'Economia, Hisenda i Innovació Grants No. SINCO2022/18146 and No. SINCO2022/6719, cofinanced by the European Union and FEDER Operational Program 2021–2027 of the Balearic Islands; the "ERDF A way of making Europe." This material is based upon work supported by NSF's LIGO Laboratory which is a major facility fully funded by the National Science Foundation.

APPENDIX A: DETAILS ON THE GENERAL GEODESIC EQUATIONS

Following Ref. [44], for geodesics in Kerr spacetime, the constants of motion E, L_z and Carter's constant Q for given orbital parameters and also the parameters of the source a and $q = m_1/m_2 = M/\mu$ are given by [using Boyer-Lindquist coordinates (r, θ, ϕ, t)]

$$\frac{\mathrm{d}r}{\mathrm{d}\tau} = R(r) = [(r^2 + a^2)E - aL_z]^2 - \Delta[\mu^2 r^2 + (L_z - aE)^2 + Q] = 0, \quad \text{(A1)}$$

$$\frac{d\theta}{d\tau} = \Theta(\theta) = Q - \left[(\mu^2 - E^2)a^2 + \frac{L_z^2}{\sin^2\theta}\right]\cos^2\theta = 0, \quad \text{(A2)}$$

where $\Delta = r^2 - 2Mr + a^2$. The roots of the equations correspond to the turning points of the radial and polar motion. For circular orbits ($e = 0$), we will need a third constraint $R'(r_0) = 0$, apart from $R(r_0) = 0$ and $\Theta(\theta_0) = 0$. Circular orbits are stable if $R''(r_0) < 0$. The radius that separates the stable and unstable orbits is known as the ISSO and hence satisfies $R''(r_0) = 0$. Thus, solving these four equations one can find the radius $r_0 = r_{\rm ISSO}$, the energy E, the orbital angular momentum L_z, and Carter's constant Q for a given system and orbital quantities.

If we use the dimensionless quantities introduced in Eq. (2.2) and rearrange $\Theta(\theta_-) = 0$, we can express the Carter constant as

$$\tilde{Q} = \cos^2\theta_- \left[\tilde{a}^2(1 - \tilde{E}^2) + \frac{\tilde{L}_z^2}{1 - \cos^2\theta_-}\right]. \quad \text{(A3)}$$

Substituting this equation in $\tilde{R}(\tilde{r})$ gives

$$\tilde{R}(\tilde{r}) = f(\tilde{r})\tilde{E}^2 - 2g(\tilde{r})\tilde{E}\,\tilde{L}_z - h(\tilde{r})\tilde{L}_z + d(\tilde{r}), \quad \text{(A4)}$$

where

$$f(\tilde{r}) = \tilde{r}^4 + \tilde{a}^2[\tilde{r}(\tilde{r} + 2) + \cos^2\theta\tilde{\Delta}], \quad \text{(A5)}$$

$$g(\tilde{r}) = 2\tilde{a}\,\tilde{r}, \quad \text{(A6)}$$

$$h(\tilde{r}) = \tilde{r}(\tilde{r} - 2) + \frac{\cos^2\theta_-}{1 - \cos^2\theta_-}\tilde{\Delta}, \quad \text{(A7)}$$

$$d(\tilde{r}) = (\tilde{r}^2 + \tilde{a}^2\cos^2\theta_-)\tilde{\Delta}, \quad \text{(A8)}$$

and one can then compute $\tilde{R}'(\tilde{r_0})$ and $\tilde{R}''(\tilde{r_0})$ from Eq. (A4). Solving these equations yields *four* solutions for the constants of motions and one fixed value for the $r_{\rm ISSO}$ in the case of circular orbits. Considering only those solutions with positive energy, we have $(\tilde{E}^{(p)}, \tilde{L}_z{}^{(p)}, \tilde{Q}^{(p)})$ and $(\tilde{E}^{(r)}, \tilde{L}_z{}^{(r)}, \tilde{Q}^{(r)})$, where p stands for prograde orbits and r stands for retrograde. It is verified that $\tilde{E}^{(p)} < \tilde{E}^{(r)}$ and $\tilde{L}_z{}^{(p)} < \tilde{L}_z{}^{(r)}$; for prograde orbits the particle has higher binding energy and corevolves with the black hole, whereas retrograde orbits usually counterrevolve.

APPENDIX B: INFORMATION CRITERIA

We do not work with an *a priori Ansatz* for our parametrized fits, but rather select the best functional form from a wide class of models. We then use information criteria to perform the model selection to avoid overfitting, following [36], where aligned spin fits for the remnant quantities are constructed. In this appendix, we describe the information criteria in more detail.

A basic performance metric for model adjustment is the RMSE. For a model of a quantity q dependent on parameters λ, and data points (λ_i, q_i) for $i = 1\ldots N$,

$$\text{RMSE[model]} = \sqrt{\frac{1}{N}\sum_{i=1}^{N}[q_i - \text{model}(\lambda_i)]^2}. \quad \text{(B1)}$$

Using only the RMSE to perform model selection is prone to overfitting. For this reason, when selecting the best model, one should penalize models according to its complexity, specifically the number of free coefficients. A widely used statistical quantity is the Akaike information criterion (AIC) [77],

$$\text{AIC} = -2\ln\mathcal{L}_{\max} + 2N_{\rm coeffs}, \quad \text{(B2)}$$

which compensates the accuracy of the fit with the number of coefficients. Here a lower value of the AIC indicates better suitability of the model. We have used the implementation of the AIC in *Mathematica*'s LinearModelFit function [75].

An alternative quantity that serves the same purpose, but has a different theoretical foundation, is the Bayesian information criterion [78],

$$\text{BIC} = -2\ln\mathcal{L}_{\max} + N_{\rm coeffs}\ln N_{\rm data}. \quad \text{(B3)}$$

In terms of performance, both criteria penalize the degeneracies between parameters and the BIC usually penalizes additional parameters more than AIC. To discern between models, a 1 unit difference is generally required, while 10 points would be decisive evidence. Further discussion on the criteria can be found in [79].

APPENDIX C: FIT FOR THE UPDATED ALIGNED RADIATED ENERGY

In this appendix, we provide the full parametrized expression for the aligned spin radiated energy used in this paper, which updates the one developed in Ref. [36].

Defining

$$\hat{S} := \frac{\chi_1 + q^2\chi_2}{1 + q^2}, \quad \text{(C1)}$$

we can write

$$
\begin{aligned}
E_{\rm AS} = {} & 0.288265\eta^5(\chi_1-\chi_2)^2 - 0.0483974\eta^2(1-1.76539\eta)\sqrt{1-4\eta}(\chi_1-\chi_2) \\
& + \frac{1393.61\eta^7 - 1160.94\eta^6 + 372.473\eta^5 - 54.0578\eta^4 + 3.33345\eta^3 + 0.44487\eta^2 + \left(1-\frac{2\sqrt{2}}{3}\right)\eta}{(1.96359\eta^2 + 0.557424\eta - 0.956935)\hat{S} + 1} \\
& [(-5.40979\eta^2 + 1.74325\eta - 0.106587)\hat{S}^6 + (0.915964\eta^2 + 0.0338535\eta - 0.0809724)\hat{S}^5 \\
& + (3.93186\eta^2 - 1.15351\eta + 0.0316422)\hat{S}^4 + (-1.16612\eta^2 + 0.379967\eta - 0.0552524)\hat{S}^3 \\
& + (-0.950876\eta^2 + 0.635553\eta - 0.173169)\hat{S}^2 + (-2.75115\eta^2 + 1.73637\eta - 0.398234)\hat{S} + 1]. \qquad \text{(C2)}
\end{aligned}
$$

APPENDIX D: EXTRAPOLATION OF THE REMNANT MODEL TOWARD EXTREME SPINS

In this appendix, we assess the extrapolation behavior of our parametrized remnant models focusing on the scenario where precession effects are maximized. Specifically, we explore spin magnitudes beyond the calibrated regime ($0.8 \leq \chi_1 \leq 1$), considering the case of in-plane configurations ($\theta_1 = \pi/2$).

Figure 17 illustrates the extrapolation results, showing a smooth continuation without exhibiting any nonphysical behavior, as well as the Kerr limit $\chi_1 \leq 1$. While these extrapolations provide valuable insights, it is important to interpret them cautiously, recognizing the need for further refinement when numerical data becomes available in the high spin magnitude regime.

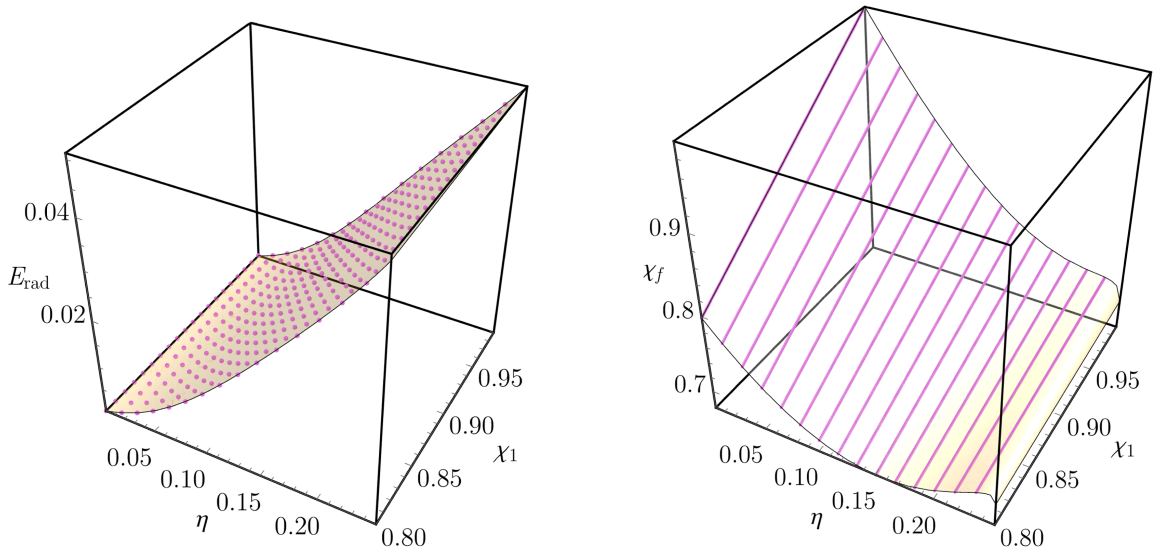

FIG. 17. Extrapolation of the remnant fits developed in Secs. III A (left) and III B (right) outside of their spin calibration regime, $0.8 \leq \chi_1 \leq 1$, for a single in-plane spin configuration ($\theta_1 = \pi/2$), where precession effects are maximized.

[1] P. Amaro-Seoane *et al.*, Living Rev. Relativity **26**, 2 (2023).
[2] The eLISA Consortium, arXiv:1305.5720.
[3] A. Antonelli, M. van de Meent, A. Buonanno, J. Steinhoff, and J. Vines, Phys. Rev. D **101**, 024024 (2020).
[4] S. Isoyama, R. Fujita, A. J. K. Chua, H. Nakano, A. Pound, and N. Sago, Phys. Rev. Lett. **128**, 231101 (2022).
[5] L. Barack and A. Pound, Rep. Prog. Phys. **82**, 016904 (2018).

[6] H. Estellés, M. Colleoni, C. García-Quirós, S. Husa, D. Keitel, M. Mateu-Lucena, M. d. L. Planas, and A. Ramos-Buades, Phys. Rev. D **105**, 084040 (2022).
[7] G. Pratten *et al.*, Phys. Rev. D **103**, 104056 (2021).
[8] H. Yu, J. Roulet, T. Venumadhav, B. Zackay, and M. Zaldarriaga, Phys. Rev. D **108**, 064059 (2023).
[9] S. Ossokine *et al.*, Phys. Rev. D **102**, 044055 (2020).
[10] A. Ramos-Buades, A. Buonanno, H. Estellés, M. Khalil, D. P. Mihaylov, S. Ossokine, L. Pompili, and M. Shiferaw, Phys. Rev. D **108**, 124037 (2023).
[11] A. Nagar *et al.*, Phys. Rev. D **98**, 104052 (2018).
[12] V. Varma, S. E. Field, M. A. Scheel, J. Blackman, D. Gerosa, L. C. Stein, L. E. Kidder, and H. P. Pfeiffer, Phys. Rev. Res. **1**, 033015 (2019).
[13] V. Varma, S. E. Field, M. A. Scheel, J. Blackman, L. E. Kidder, and H. P. Pfeiffer, Phys. Rev. D **99**, 064045 (2019).
[14] B. P. Abbott *et al.* (LIGO Scientific and Virgo Collaborations), Phys. Rev. X **9**, 031040 (2019).
[15] R. Abbott *et al.* (LIGO Scientific and Virgo Collaborations), Phys. Rev. X **11**, 021053 (2021).
[16] R. Abbott *et al.* (LIGO Scientific and Virgo Collaborations), Phys. Rev. D **109**, 022001 (2024).
[17] R. Abbott *et al.* (KAGRA, Virgo, and LIGO Scientific Collaborations), Phys. Rev. X **13**, 041039 (2023).
[18] E. Hamilton, L. London, J. E. Thompson, E. Fauchon-Jones, M. Hannam, C. Kalaghatgi, S. Khan, F. Pannarale, and A. Vano-Vinuales, Phys. Rev. D **104**, 124027 (2021).
[19] S. Ghosh, P. Kolitsidou, and M. Hannam, Phys. Rev. D **109**, 024061 (2024).
[20] J. E. Thompson, E. Hamilton, L. London, S. Ghosh, P. Kolitsidou, C. Hoy, and M. Hannam, Phys. Rev. D **109**, 063012 (2024).
[21] J. Healy and C. O. Lousto, Phys. Rev. D **105**, 124010 (2022).
[22] M. Boyle *et al.*, Classical Quantum Gravity **36**, 195006 (2019).
[23] E. Hamilton *et al.*, Phys. Rev. D **109**, 044032 (2024).
[24] D. Ferguson *et al.*, arXiv:2309.00262.
[25] A. Gonzalez *et al.*, Classical Quantum Gravity **40**, 085011 (2023).
[26] C. O. Lousto and J. Healy, Classical Quantum Gravity **40**, 09LT01 (2023).
[27] M. Fernando, D. Neilsen, Y. Zlochower, E. W. Hirschmann, and H. Sundar, Phys. Rev. D **107**, 064035 (2023).
[28] A. Le Tiec *et al.*, Phys. Rev. D **88**, 124027 (2013).
[29] A. Albertini, A. Nagar, A. Pound, N. Warburton, B. Wardell, L. Durkan, and J. Miller, Phys. Rev. D **106**, 084061 (2022).
[30] B. Wardell, A. Pound, N. Warburton, J. Miller, L. Durkan, and A. Le Tiec, Phys. Rev. Lett. **130**, 241402 (2023).
[31] T. Islam, S. E. Field, S. A. Hughes, G. Khanna, V. Varma, M. Giesler, M. A. Scheel, L. E. Kidder, and H. P. Pfeiffer, Phys. Rev. D **106**, 104025 (2022).
[32] T. Islam, S. E. Field, and G. Khanna, Phys. Rev. D **108**, 064048 (2023).
[33] T. Islam, Phys. Rev. D **108**, 044013 (2023).
[34] C. Garcia-Quiros, M. Colleoni, S. Husa, H. Estelles, G. Pratten, A. Ramos-Buades, M. Mateu-Lucena, and R. Jaume, Phys. Rev. D **102**, 064002 (2020).
[35] H. Estelles, S. Husa, M. Colleoni, D. Keitel, M. Mateu-Lucena, C. Garcia-Quiros, A. Ramos-Buades, and A. Borchers, Phys. Rev. D **105**, 084039 (2022).
[36] X. Jiménez-Forteza, D. Keitel, S. Husa, M. Hannam, S. Khan, and M. Pürrer, Phys. Rev. D **95**, 064024 (2017).
[37] J. Healy, C. O. Lousto, and Y. Zlochower, Phys. Rev. D **90**, 104004 (2014).
[38] Y. Zlochower and C. O. Lousto, Phys. Rev. D **92**, 024022 (2015).
[39] F. Hofmann, E. Barausse, and L. Rezzolla, Astrophys. J. Lett. **825**, L19 (2016).
[40] M. Boschini *et al.*, Phys. Rev. D **108**, 084015 (2023).
[41] L. Haegel and S. Husa, Classical Quantum Gravity **37**, 135005 (2020).
[42] A. Apte and S. A. Hughes, Phys. Rev. D **100**, 084031 (2019).
[43] H. Lim, G. Khanna, A. Apte, and S. A. Hughes, Phys. Rev. D **100**, 084032 (2019).
[44] W. Schmidt, Classical Quantum Gravity **19**, 2743 (2002).
[45] B. Bruegmann, J. A. Gonzalez, M. Hannam, S. Husa, and U. Sperhake, Phys. Rev. D **77**, 124047 (2008).
[46] J. Mathews, A. Pound, and B. Wardell, Phys. Rev. D **105**, 084031 (2022).
[47] SpEC code, https://www.black-holes.org/code/SpEC.html.
[48] B. Brügmann, J. A. González, M. Hannam, S. Husa, U. Sperhake, and W. Tichy, Phys. Rev. D **77**, 024027 (2008).
[49] S. Husa, J. A. González, M. Hannam, B. Brügmann, and U. Sperhake, Classical Quantum Gravity **25**, 105006 (2008).
[50] L. Werneck *et al.*, The Einstein Toolkit, to find out more, visit http://einsteintoolkit.org (2023).
[51] S. Ossokine, M. Boyle, L. E. Kidder, H. P. Pfeiffer, M. A. Scheel, and B. Szilágyi, Phys. Rev. D **92**, 104028 (2015).
[52] F. Pretorius, Classical Quantum Gravity **22**, 425 (2005).
[53] J. W. York, Jr., Phys. Rev. Lett. **82**, 1350 (1999).
[54] G. Lovelace, R. Owen, H. P. Pfeiffer, and T. Chu, Phys. Rev. D **78**, 084017 (2008).
[55] J. M. Bowen and J. W. York, Phys. Rev. D **21**, 2047 (1980).
[56] A. Ramos-Buades, S. Husa, and G. Pratten, Phys. Rev. D **99**, 023003 (2019).
[57] D. Pollney, C. Reisswig, E. Schnetter, N. Dorband, and P. Diener, Phys. Rev. D **83**, 044045 (2011).
[58] J. Thornburg, Classical Quantum Gravity **21**, 743 (2004).
[59] R. H. Boyer and R. W. Lindquist, J. Math. Phys. (N.Y.) **8**, 265 (1967).
[60] S. Drasco and S. A. Hughes, Phys. Rev. D **73**, 024027 (2006); **88**, 109905 (2013); **90**, 109905 (2014).
[61] Black Hole Perturbation Toolkit, https://bhptoolkit.org/.
[62] A. Ori and K. S. Thorne, Phys. Rev. D **62**, 124022 (2000).
[63] P. A. Sundararajan, G. Khanna, and S. A. Hughes, Phys. Rev. D **76**, 104005 (2007).
[64] P. A. Sundararajan, G. Khanna, S. A. Hughes, and S. Drasco, Phys. Rev. D **78**, 024022 (2008).
[65] P. Schmidt, M. Hannam, S. Husa, and P. Ajith, Phys. Rev. D **84**, 024046 (2011).
[66] P. Schmidt, M. Hannam, and S. Husa, Phys. Rev. D **86**, 104063 (2012).
[67] M. Boyle, R. Owen, and H. P. Pfeiffer, Phys. Rev. D **84**, 124011 (2011).

[68] L. E. Kidder, Phys. Rev. D **52**, 821 (1995).
[69] P. Schmidt, F. Ohme, and M. Hannam, Phys. Rev. D **91**, 024043 (2015).
[70] M. Cabero, A. B. Nielsen, A. P. Lundgren, and C. D. Capano, Phys. Rev. D **95**, 064016 (2017).
[71] N. K. Johnson-McDaniel, S. Kulkarni, and A. Gupta, Phys. Rev. D **106**, 023001 (2022).
[72] D. Kennefick and A. Ori, Phys. Rev. D **53**, 4319 (1996).
[73] L. C. Stein and N. Warburton, Phys. Rev. D **101**, 064007 (2020).
[74] G. Pratten *et al.*, Phys. Rev. D **103**, 104056 (2021).
[75] Wolfram Research, `LinearModelFit`, https://reference.wolfram.com/language/ref/LinearModelFit.html (2008) (accessed: January 12, 2024).
[76] Wolfram Research, `Fit`, https://reference.wolfram.com/language/ref/Fit.html (2019) (accessed: January 15, 2024).
[77] H. Akaike, IEEE Trans. Autom. Control **19**, 716 (1974).
[78] G. Schwarz, Ann. Stat. **6**, 461 (1978).
[79] A. R. Liddle, Mon. Not. R. Astron. Soc. **377**, L74 (2007).